

## Interaction between plasma synthetic jet and subsonic turbulent boundary layer

Zong, H.; Kotsonis, Marios

**DOI**

[10.1063/1.4979527](https://doi.org/10.1063/1.4979527)

**Publication date**

2017

**Document Version**

Accepted author manuscript

**Published in**

Physics of Fluids

**Citation (APA)**

Zong, H., & Kotsonis, M. (2017). Interaction between plasma synthetic jet and subsonic turbulent boundary layer. *Physics of Fluids*, 29(4), Article 045104. <https://doi.org/10.1063/1.4979527>

**Important note**

To cite this publication, please use the final published version (if applicable).  
Please check the document version above.

**Copyright**

Other than for strictly personal use, it is not permitted to download, forward or distribute the text or part of it, without the consent of the author(s) and/or copyright holder(s), unless the work is under an open content license such as Creative Commons.

**Takedown policy**

Please contact us and provide details if you believe this document breaches copyrights.  
We will remove access to the work immediately and investigate your claim.

# Interaction between Plasma Synthetic Jet and Subsonic Turbulent Boundary Layer

Haohua Zong\* and Marios Kotsonis

*Faculty of Aerospace Engineering, Delft University of Technology, Delft 2629 HS, Netherlands*

**Abstract:** This paper experimentally investigates the interaction between a plasma synthetic jet (PSJ) and a subsonic turbulent boundary layer (TBL) using a hotwire anemometer and a phase-locked Particle Imaging Velocimetry (PIV). The PSJ is interacting with a fully developed turbulent boundary layer developing on the flat wall of a square wind tunnel section of 1.7 m length. The Reynolds number based on the freestream velocity ( $U_\infty=20$  m/s) and the boundary layer thickness ( $\delta_{99}=34.5$  mm) at the location of interaction is 44400. A large-volume ( $1696$  mm<sup>3</sup>) three-electrode plasma synthetic jet actuator (PSJA) with a round exit orifice ( $D=2$  mm) is adopted to produce high-speed (92 m/s) and short-duration ( $T_{jet}=1$  ms) pulsed jets. The exit velocity variation of the adopted PSJA in crossflow is shown to remain almost identical to that in quiescent conditions. However, the flow structures emanating from the interaction between the PSJ and the TBL are significantly different from what observed in quiescent conditions. In the midspan  $xy$  plane ( $z=0$  mm), the erupted jet body initially follows a wall-normal trajectory accompanied by the formation of a distinctive front vortex ring. After three convective time scales the jet bends to the crossflow, thus limiting the peak penetration depth to approximately  $0.58\delta_{99}$ . Comparison of the normalized jet trajectories indicates that the penetration ability of the PSJ is less than steady jets with the same *momentum flow velocity*. Prior to the jet diminishing, a recirculation region is observed in the leeward side of the jet body, experiencing first an expansion and then a contraction in the area. In the cross-stream  $yz$  plane, the signature structure of jets in crossflow, the counter-rotating vortex pair (CVP), transports high-momentum flow from the outer layer to the near-wall region, leading to a fuller velocity profile and a drop in the boundary layer shape factor (1.3 to 1.2). In contrast to steady jets, the CVP produced by the PSJ exhibits a prominent spatiotemporal behaviour. The residence time of the CVP is estimated as the jet duration time, while the maximum extent of the affected flow in the three coordinate directions ( $x$ ,  $y$  and  $z$ ) is approximately  $32D$ ,  $8.5D$  and  $10D$ , respectively. An extremely high level of turbulent kinetic energy (TKE) production is shown in the jet shear-layer, front vortex ring and CVP, of which the contribution of the streamwise Reynolds normal stress is dominant. Finally, a conceptual model of the interaction between the PSJ and the TBL is proposed.

**Keywords:** synthetic jet; actuator; crossflow; turbulent boundary layer

## 1. Introduction

### 1.1 Jets in crossflow (JICF)

The term *Jets in Crossflow* (JICF), also known as transverse jets, refers to the flow phenomena developing during interaction of the jet flow emitting from an orifice with the external flow across the orifice (Margason 1993). During the interaction, the emitted jets bend to the crossflow and abundant vortical structures are exhibited including horseshoe vortices, shear-layer vortices, wake vortices, hanging vortices and a counter-rotating vortex pair (CVP) (Broadwell & Breidenthal 1984, Yuan et al. 1999, Cortelezzi & Karagozian 2001). Extensive applications of JICF can be found in engineering, including gas film cooling on high-temperature turbine blade surfaces, fuel injection in thermal engine combustors, thrust vectoring technology for missiles and active flow control on airfoils, as reviewed by Margason (1993), Karagozian (2010) and Mahesh (2013).

Different applications pivot around diverse inherent features of JICF. In supersonic combustion chambers, the jet penetration ability, spreading rate and entrainment rate are of paramount importance to yield efficient mixing between fuel and air in timescales of several milliseconds (Fuller et al. 1992). However, in separation control applications, the signature vortex structure, namely the CVP, receives significant attention (Cortelezzi & Karagozian 2001). The CVP is orientated in the quasi-streamwise direction and bears similar features as the hairpin vortices in a turbulent boundary layer (TBL) (Adrian 2007). Specifically, under the induced effects of the CVP, the high-momentum flow in the outer layer is transported to the near-wall region and mixed with the low-momentum fluids, leading to an energised boundary layer with fuller velocity profile and thus an enhanced capability to resist against the adverse pressure gradient associated with flow separation.

### 1.2 Steady jets vs. synthetic jets

Steady jets were investigated much earlier than synthetic jets by the flow control community. Johnston & Nishi (1990) and Compton & Johnston (1992) indicate that by skewing and inclining the jet angle, a single dominant streamwise vortex, similar to that created by a weak solid vortex generator, can be produced by steady jets in crossflow. Thus, JICF are also named as vortex generator jets. The steady-blowing vortex generator jet was tested by Bons, Sondergaard & Rivir (1999) to control the flow separation on the suction surface of turbine blades. A clear decrease in pressure loss coefficient was obtained at low (<1%) and moderate (4%) levels of freestream turbulence. However, a considerable blowing ratio and mass flux are necessary for such effect. This imposes significant challenges on industrial applications such as aircrafts, as the penalties incurred by carrying external or internal pressurized gas tanks for supplying the jets may go beyond the benefits brought by flow separation suppression. Similar restrictions might also apply in the case of extracting bleed air from the compression stages of the engine.

In an effort to relax the mass flux requirement (external gas source requirement or bleed air), pulsed jets and synthetic jets were successively proposed and applied for separation control by Seifert, Darabi & Wygnanski (1996) and Smith & Glezer (1998). In a typical demonstration (freestream velocity: 32 m/s), the stall angle of a NACA four-digit series symmetric airfoil was postponed from 5

degrees to 17.5 degrees by piezoelectrically driven synthetic jet actuators, accompanied by a 100% increment in the lift coefficient and a 45% decrement in the drag coefficient (Amitay et al. 2001).

While laboratory tests at low Reynolds numbers give encouraging results, conventional synthetic jets formed by acoustic waves or oscillating diaphragms are not adequate to manipulate high-Reynolds-number supersonic flows. Early investigations from Glezer & Amitay (2002) showed that the peak jet velocity of piezoelectrically driven synthetic jet actuators is typically less than 60 m/s, due to the constraints on the power input of piezoelectric membranes. By driving the actuator at the diaphragm resonance frequency and using a dual disc configuration, Gomes (2009) and Buren et al. (2016) managed to improve the peak jet velocity to approximately 200 m/s. Although promising, this velocity magnitude still remains in the high-subsonic category and declines significantly in the condition of off-resonance-frequency operation, thus limiting the effective dynamic range of the actuator.

In 2006, Crittenden & Glezer proposed a piston/cylinder synthetic jet actuator capable of producing supersonic jets (~600 m/s). Nevertheless, this pure mechanical design has a noticeable disadvantage of complex structures and low working frequency (<200 Hz).

### *1.3 Plasma synthetic jet (PSJ): characterisation and application*

In 2003, a new-concept zero-net-mass-flow actuator, namely the plasma synthetic jet actuator (PSJA), was proposed and designed by Grossman, Cybyk & Vanwie. Similar to other plasma actuators, PSJA has an inherently fast response and simple structure, usually comprised of several discharge electrodes and a closed cavity with an exit orifice (diameter: 0.5-3 mm). A morphological deviation from conventional synthetic jets is the absence of any moving components. Nanosecond pulse discharge (Zong et al. 2015), pulsed DC discharge (Shin 2010) and capacitive discharge (Belinger et al. 2011) can be utilized to rapidly pressurize the cavity gas, depending on the cavity volume. Narayanaswamy, Raja & Clemens (2010) investigated a small-cavity PSJA (~22 mm<sup>3</sup>) fed by the pulsed DC discharge (discharge energy: 30 mJ). A high-velocity (250 m/s) pulsed jet is generated consistently at 5 kHz. Reedy et al. (2013) measured the flow field of a medium-volume PSJA (~183 mm<sup>3</sup>) using PIV. The peak jet velocity recorded in the single-shot mode was measured as high as 496 m/s. For large-volume PSJA (>1000 mm<sup>3</sup>) fed by capacitive discharge (discharge energy: 2.6 J), a peak jet velocity of 345 m/s and a jet duration time longer than 2.5 ms were reported by Wang et al. (2014).

Recent characterisation studies by Golbabaie-Asl, Knight & Wilkinson (2015) and Zong et al. (2016) suggest that PSJA as an electromechanical device exhibits a rather low energy conversion efficiency (<10%). Nevertheless, the unique combination of high jet velocity and high actuation frequency still motivates the application of PSJA to scenarios such as shock wave manipulation (Emerick et al. 2014), shock wave\boundary layer interaction control (SWBLI) (Narayanaswamy et al. 2010 & 2012), and flight control (Anderson & Knight 2012).

Narayanaswamy, Raja & Clemens (2010 & 2012) tested the performance of PSJA in a Mach 3 crossflow. They showed that the produced pulsed jets have a penetration length of about 1.5 boundary-

layer thickness, and contribute to 30% reduction of the pressure fluctuation associated with the large-scale separated flow in SWBLI at a Strouhal number of approximately 0.04. Greene et al. (2015) adopted a similar experimental setup and examined several skew and pitch angles of the pulsed jets. The 20° pitch and 0° skew jets performed the best among all tested cases. The distance between the separation line and the compression ramp corner was reduced by up to 40%, while the shape factor of the downstream reattached boundary layer was decreased from 1.57 to 1.49, suggesting enhanced mixing. Emerick et al. (2014) mounted a PSJA array in a Mach 1.5 crossflow, and a maximum shock wave deflection angle of 5° was observed in single-shot operation. In a subsonic study (freestream velocity: 40 m/s), trailing edge separation of a NACA 0015 airfoil was effectively weakened by a PSJA array and 19% drag reduction was observed (Caruana et al. 2013).

#### *1.4 Background of the current study: physics of PSJ in crossflow*

Although positive results are demonstrated in the aforementioned preliminary flow control attempts, the flow scenario of PSJ in crossflow remains unclear. In contrast to the steady jets, plasma synthetic jets demonstrate a highly dynamic behaviour. The jet exit velocity of the PSJA changes dramatically in one period (Zong & Kotsonis 2016a). As a result, the major flow structures produced by the interaction between PSJ and crossflow may exhibit strong spatiotemporal behaviours. In the case of conventional synthetic jets in crossflow, Buren et al. (2016a & 2016b) observed a recirculation region downstream of the orifice and a streamwise vortex pair in the far-field. For the interaction between PSJ and crossflow, identifying the similar dominant flow structures at different phases of the interaction and further investigating the pertinent spatiotemporal scales are essential not only to reveal the underlying physics but also to optimize the actuation parameters.

This study takes the first step towards tackling this issue, beginning with the nominal case of the interaction between a wall-normal PSJ and a subsonic TBL in single-shot mode. Phase-locked Particle Image Velocimetry (PIV) measurements in multiple planes are deployed to capture the evolution of three-dimensional flow structures at different phases. In *Section 2*, the utilized experimental facilities including the PSJA, wind tunnel, hotwire anemometer and PIV systems are introduced. PIV data validation is performed in *Section 3*. From *Section 4* to *Section 5*, the phase-averaged flow organisation, and the turbulent kinetic energy distribution are presented successively. In addition, a conceptual model of PSJ in crossflow is drafted in *Section 6*.

## **2. Experimental setup**

### *2.1 Actuator and power supply*

For the purpose of this study, a three-electrode plasma synthetic jet actuator is adopted, mainly composed of a ceramic cavity and a metal cap. The ceramic cavity shown in Figure 1 is in a cylindrical shape with internal height of 15 mm and internal diameter of 12 mm, resulting in a cavity volume of 1696 mm<sup>3</sup>. The cap of this actuator, which accommodates the exit orifice, is fabricated as a metal disk flush-mounted with the bottom wall of the wind tunnel test section, as will be shown in *Section 2.2*. Four holes are drilled equidistantly in the circumferential direction, in a plane located 7.5 mm from the cavity bottom. Three tungsten needles are inserted into the cavity, serving as anode,

cathode and trigger electrode, respectively. The remaining hole is designed for the intra-cavity PIV seeding (Zong & Kotsonis 2016a). The distance from the actuator axisymmetry axis to the anode, cathode and trigger electrode is fixed at 1 mm, 2 mm and 0.5 mm, respectively. A weak trigger discharge and a strong capacitive discharge are initiated sequentially in the cavity by a high-voltage amplifier (Trek Model 20/20C), in conjunction with several electrical components. Detailed information on the power supply system can be found in Zong & Kotsonis (2016a).

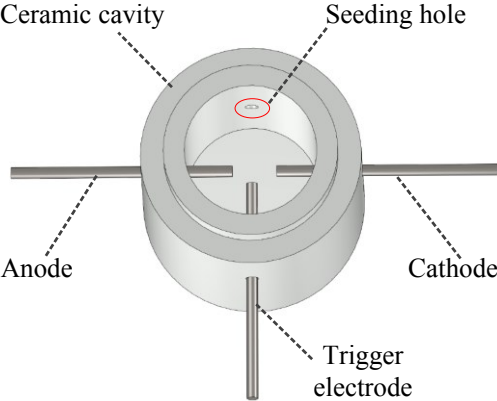


FIGURE 1. Actuator structure

2.2 Wind tunnel and test section

The experiments are carried out in the W-tunnel of Delft University of Technology. The W-tunnel is an open-return tunnel, with interchangeable contraction parts and test sections. A square test section of 0.5m×0.5m dimension and 3 m length is installed for the purpose of this study, resulting in a maximum velocity of 25 m/s and a turbulence level of about 0.5%. As shown in Figure 2, the test section is smoothly connected with the contraction part and fabricated using plexiglass to facilitate the optical measurements. In this study, the freestream velocity ( $U_\infty$ ) is kept constant at 20 m/s. Atmospheric pressure and temperature of the incoming flow are measured by a digital barometer and a thermocouple respectively. At the time of measurement, atmospheric pressure and flow temperature were approximately 101000 Pa and 288 K, respectively.

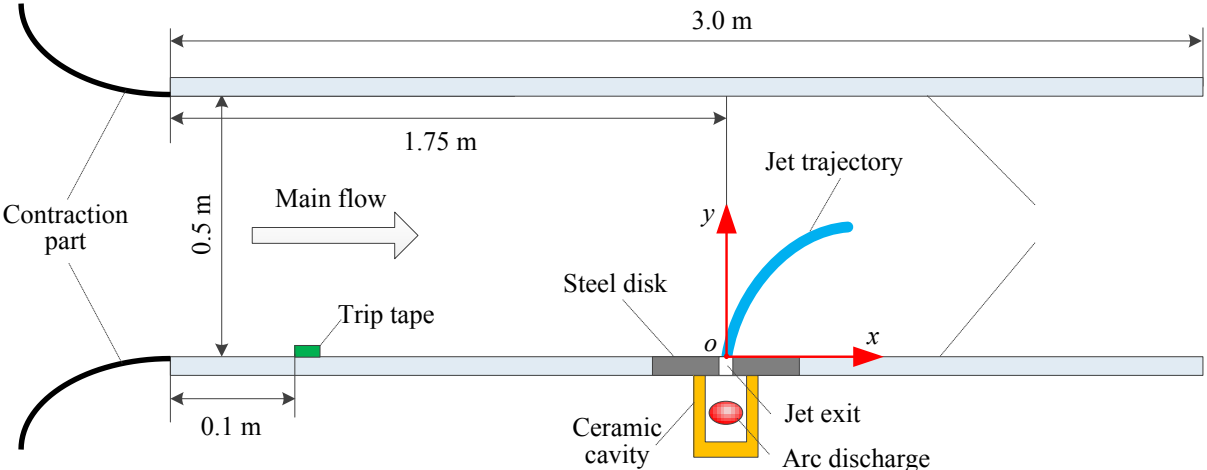


FIGURE 2. Schematic diagram of test section

The boundary layer developing naturally on the bottom wall of the contraction part is tripped by a zigzag tape located at 0.1 m downstream of the leading edge of the test section. A steel disk (diameter: 0.11 m) is flush-mounted in the bottom plate. The ceramic cavity shown in Figure 1 is assembled in the steel disk via a step groove. In the centre of the steel disk, a round orifice (diameter: 2 mm) is drilled, serving as the jet exit. The distance from the jet exit centre to the leading edge of the test section is 1.75 m. A coordinate system is in reference to the jet exit centre, with  $x$ ,  $y$  and  $z$  axis along the streamwise, wall-normal and spanwise direction, respectively.

The bottom wall of the test section is furnished with 16 pressure taps (diameter: 0.4 mm) located between  $x=-0.75$  m and  $x=0.25$  m to acquire the pressure distribution. Additionally, a Pitot-static tube is mounted at  $x=-0.15$  m to obtain the dynamic pressure of the uninterrupted freestream flow ( $0.5\rho U_\infty^2$ ). The pressure signals are scanned by a mechanical pressure scanivalve. A high-accuracy pressure transducer (Mensor, Model 2101), together with Labview software, realizes the transformation and the recording of pressure signals. The recording length and the acquisition frequency are set as 5 s and 10 Hz, respectively. For the conditions of the current study ( $U_\infty=20$  m/s), the measured pressure distribution on the bottom wall (denoted by  $\Delta p$ ) is shown in Figure 3. The ratio of  $\Delta p$  to  $0.5\rho U_\infty^2$  defines the pressure coefficient. Due to the growth of boundary layer, the effective flow area drops consistently along the streamwise direction. This results in a mildly increasing freestream velocity and a decreasing wall pressure. The peak value of the pressure coefficient is approximately -0.05. The PIV measurements are performed between  $-0.02$  m  $< x < 0.1$  m. In this interval, the pressure coefficient changes less than 1%. Thus, the turbulent boundary layer (TBL) investigated in this paper can be roughly treated as a zero-pressure-gradient TBL.

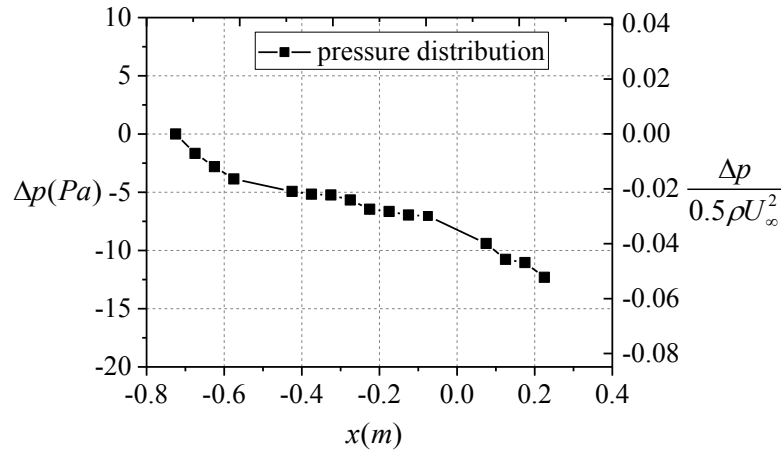


FIGURE 3. Pressure distribution along the bottom wall of the test section. The static pressure at  $x=-0.75$  m is chosen as the reference pressure.

### 2.3. Hotwire anemometer and Particle Image Velocimetry

Hotwire measurements are performed in the baseline non-actuated case, in order to reference and validate the PIV data. A single-wire boundary layer probe (Dantec Dynamics, P15), operated by a TSI IFA-300 constant temperature bridge working in constant-temperature mode, is utilized to obtain the boundary layer velocity profile at  $x=50$  mm in the  $xy$  plane ( $z=0$  mm). The wire calibration is

performed in situ in a velocity range of 0-25 m/s, and the calibration curve is fitted by a fourth order polynomial, with a maximum relative error less than 0.6%. In addition, atmospheric pressure and temperature corrections are applied to the calibration. In  $y$ -direction, 60 measurement stations are selected to fully restore the boundary layer velocity profile. An automated traversing system with accuracy of 2.5  $\mu\text{m}$ , is adopted to realize the probe motion in  $y$ -direction. During the recording, the sampling frequency and the recording time are fixed as 50 kHz and 5 s respectively, ensuing full statistical convergence.

The adopted PIV system is mainly composed of a single-head Nd:YAG laser (Quantel EverGreen, peak pulse energy: 200 mJ), two LaVision digital CCD cameras (Imager Pro LX, resolution: 3248 $\times$ 4872 pixels, pixel pitch: 7.4 $\times$ 7.4  $\mu\text{m}$ ) and a programmable timing unit (PTU9). Depending on the measurement plane, a 3-component (3C) stereo PIV measurement or 2-component (2C) planar PIV measurement with two side-by-side cameras is performed, as shown in Figure 4. By virtue of two spherical and one cylindrical lenses, the laser beam emitted from the laser head is finally shaped into a thin sheet (thickness: 0.6 mm for planar PIV and 1 mm for stereo PIV). Each camera is equipped with a 200 mm macro lens (Nikon, Micro Nikkor). The optical aperture of the lenses ( $f\#$ ) is fixed to 8 and 11 respectively during planar and stereo PIV measurements to guarantee all the illuminated particles are in focus. The particle image diameter is approximately 2-3 pixels. The laser and the two cameras are fixed on a two-axis traversing bed (accuracy: 2.5  $\mu\text{m}$ ), facilitating the change of measurement planes in  $x$ -direction and  $z$ -direction. In total, 6 measurement planes are selected to restore the 3D flow field, as listed in Table 1.

Table 1. Overview of PIV measurement parameters

Measurement plane	Measurement type	Location (mm)	FOV( $\text{mm}^2$ )	Spatial resolution	Magnification factor
$xy$ plane	2C-planar PIV	$z=0$	41 $\times$ 118	9.8 vectors/mm	0.54
$yz$ plane	3C-stereo PIV	$x=5, 10, 20, 30, 40$	71 $\times$ 73	5.7 vectors/mm	0.30

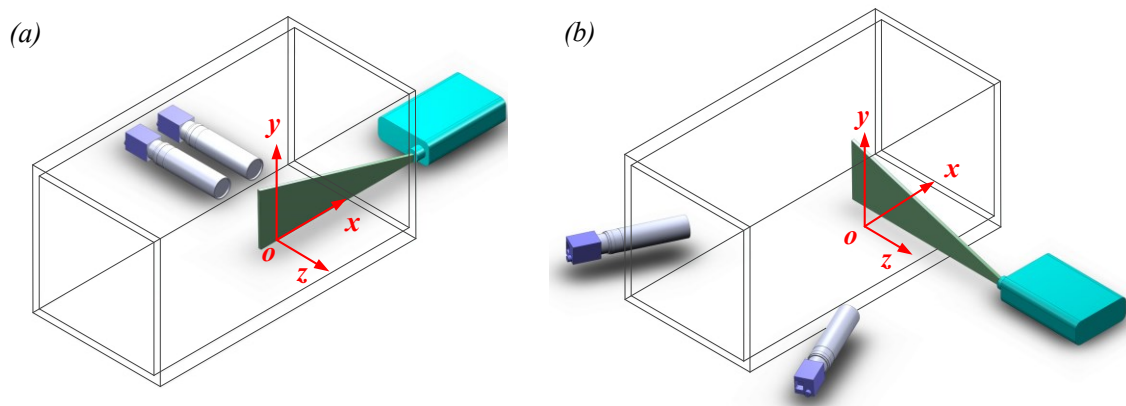


FIGURE 4. (a) 2C-planar PIV measurement setup in the  $xy$  plane and (b) 3C-stereo PIV measurement setup in the  $yz$  plane.

Regarding the flow seeding, two schemes are adopted. The primary system provides seeding by a SAFEX fog generator located in the setting chamber of the wind tunnel, using a working fluid of water-glycol mixture, producing particles of approximately 1  $\mu\text{m}$  mean diameter. A separate, secondary seeding scheme proposed by Zong & Kotsonis (2016a) is inherited, to overcome the problem of low seeding density in the jet core (Ko et al. 2010). Through the secondary system, the actuator cavity is seeded with dielectric mineral oil particles (Shell Ondina) of 1.5  $\mu\text{m}$  mean diameter, generated by an atomizer (TSI 9302). To minimise possible interference between the intra-cavity seeding and the developing jet, the intra-cavity seeding is switched off prior to the discharge by a fast-response solenoid valve (FESTO, MHJ10), synchronised to the PIV acquisition.

In order to capture the spatiotemporal evolution of the PSJ in the turbulent crossflow, all associated systems including the discharge, seeding and PIV are synchronized, working in a phase-locked mode. The synchronization is implemented by Labview software. For each measurement plane, several time delays between the discharge initiation and the PIV acquisition (denoted as  $t$ ) are selected to execute the measurement. For each time delay (phase), 500 image pairs are recorded. In *Section 3.1*, a simple convergence study is performed to demonstrate statistical convergence of the phase-averaged measurements. LaVision Davis 8.3 software is used to record and process the image pairs. The interrogation window used in the final pass has a size of  $32 \times 32$  pixels<sup>2</sup> and an overlapping ratio of 75%. Detailed values of the field of view (FOV), spatial resolution and magnification factor pertaining to each measurement plane are available in Table 1.

### 3. PIV data validation

Prior to further analysis, it is necessary to define the adopted symbol convention for this study. The instantaneous velocity, phase-averaged velocity and fluctuation velocity are denoted by  $U_i$ ,  $\bar{U}_i$  and  $u_i$  respectively, where the subscript  $i$  can be either of the three coordinate components ( $x$ ,  $y$ ,  $z$ ).  $\overline{u_i u_j}$  is the Reynolds stress.  $k$  stands for the turbulent kinetic energy.  $\delta_v$ ,  $u_\tau$  and  $y^+$  represent the viscous length scale, friction velocity and wall unit respectively.  $\varepsilon$  and  $\zeta$  denote measurement errors.  $D$  is the orifice diameter.  $\delta_{99}$  is the boundary layer thickness determined by 99% of the freestream velocity. Other symbols will be introduced in their first occurrence.

#### 3.1 PIV statistical convergence validation

A PIV convergence study is performed in the  $xy$  measurement plane ( $z=0$  mm) for the non-actuated case. 1000 vector fields are recorded. The statistic quantities analysed include the ensemble-averaged velocity and Reynolds stresses. At  $x=0$  mm, four monitor points are placed at different  $y$ -coordinates ( $y=1\text{mm}$ ,  $5\text{mm}$ ,  $10\text{mm}$  and  $20$  mm), denoted as P1-P4 respectively. As the ensemble-averaged velocity is relatively faster to converge compared with the Reynolds stresses, only the variation of  $\overline{u_x u_x}$  and  $\overline{u_x u_y}$  with sample number ( $N$ ) is detailed here. Regardless of the monitor location,  $\overline{u_x u_x}$  and  $\overline{u_x u_y}$  largely converge for  $N > 400$  (less than 6% for  $\overline{u_x u_x}$ , not shown). Thus, an ensemble size of 500 is chosen in this study as a compromise between the measurement time and the statistical convergence.

### 3.2 Comparison of PIV and hotwire measurements

The hotwire probe used is a single-sensor probe, and as such the measured velocity ( $U_{xy}$ ) is actually the Euclidean sum of the streamwise and wall-normal velocity,  $U_{xy} = \sqrt{U_x^2 + U_y^2}$ . The fluctuation of  $U_{xy}$  is denoted as  $u_{xy}$ . Based on the measured velocity profiles,  $\delta_{99}$  is determined to be 34.5 mm. The variations of  $\overline{U_{xy}}$  at  $x=50$  mm,  $z=0$  mm determined by both PIV and hotwire measurements are shown in Figure 5 (a) for comparison.

The two velocity curves agree well in the outer layer ( $y/\delta_{99} > 0.03$ ). However at  $y/\delta_{99} < 0.03$ , the velocity measured by hotwire is slightly lower than PIV. This discrepancy can be attributed to the finite spatial resolution in PIV measurement, which is largely affected by the interrogation window size in the final pass (approximately 0.5 mm in this study). The interrogation window behaves essentially as a spatial low pass filter, and the velocity determined by the cross-correlation operation is in fact the spatially-averaged velocity in the interrogation window (Scarano 2003). In the outer layer, this spatial-averaging effect is not so significant since the velocity changes smoothly. However in the near-wall region, the measured velocity profile can be slightly distorted due to the large spatial velocity gradient. In the case of zero-pressure-gradient boundary layer, the profile of  $u_{xy}$  is a convex function of the  $y$ -coordinate (Wu & Moin 2009). Thus, the spatially-averaged value should be larger than the actual value. This is confirmed by the positively biased PIV results shown in Figure 5 (a).

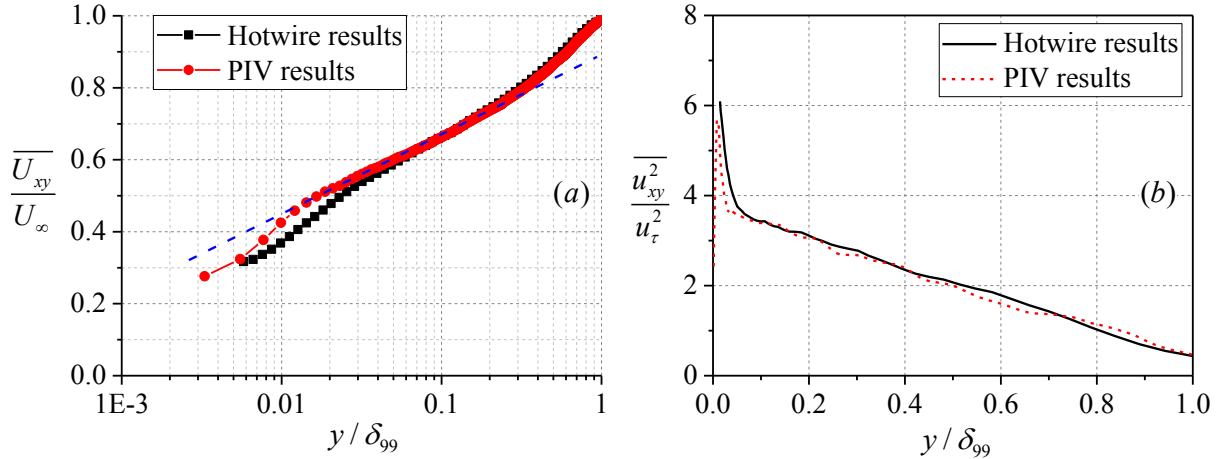


FIGURE 5. Comparison between hotwire results and PIV results at  $x=50$  mm,  $z=0$  mm. (a) Normalized boundary layer velocity profile; The blue dash line is used to determine the wall friction velocity  $u_\tau$ . (b) Reynolds shear stress normalized by  $u_\tau^2$ .

Between  $y/\delta_{99}=0.03$  and  $y/\delta_{99}=0.3$ , PIV and hotwire data collapse on the same straight line. This region corresponds to the log layer (Kline, Coles & Hirst 1969). In the log layer, the velocity profile can be accurately described by the following equation.

$$\frac{\overline{U_{xy}}}{u_\tau} = \frac{1}{\kappa} \ln\left(\frac{y}{\delta_v}\right) + B \quad (1)$$

where,  $\kappa$  is the Von Karman constant (0.41). Theoretically, the slope of the blue dash line shown in Figure 5 (a) is  $u_\tau / \kappa$ . By comparing this theoretical slope with the fitted value,  $u_\tau$  is determined to be

0.79 m/s for the present study and measurement location. The corresponding viscous length scale and time scale are 0.019 mm and 0.024 ms respectively. Choosing  $\delta_{99}$  as the reference length scale, the Reynolds numbers based on  $U_\infty$  and  $u_\tau$  are 44400 and 2060 respectively. The position of the measurement point closest to the wall is 6 and 10.5 in wall coordinates (inner scale) for PIV and hot wire respectively. In addition, the variation of  $\overline{u_{xy}^2}$  is shown in Figure 5 (b) as a function of the outer scale. The two curves show a considerable agreement. A discrepancy exists in the hotwire results not capturing the drop of  $\overline{u_{xy}^2}$  in the viscous wall region. The basic changing trend of  $\overline{u_{xy}^2}$  reported here is similar to that obtained in the channel flow (Bernardini, Pirozzoli & Orlandi 2014).

#### 4. Phase-averaged flow organization

##### 4.1 *xy* plane

Phase-averaged flow fields in the *xy* plane ( $z=0$  mm) are shown in Figure 6.  $U_\infty$  and  $D$  are used to normalize the time delay, resulting in a nondimensional convective time scale  $tU_\infty/D$ . At  $tU_\infty/D=2$  ( $t=200 \mu s$ ), a nominally wall-normal high-speed jet is expelled abruptly from the actuator, with a peak velocity of  $4.6U_\infty$  (92 m/s). As a result of this abrupt eruption, a distinctive starting vortex ring (also termed as front vortex ring) is shed from the orifice opening, experiencing an upward propagation (Cantwell 1986). A small portion of the fluid in the crossflow is entrained towards the upstanding jet by the front vortex ring, while the majority of the freestream flow bulk bypasses the high-speed jet as a solid protrusion. Despite the presence of the external flow, the incipient flow topology after discharge shares much similarity with that in the quiescent condition (Zong & Kotsonis 2016a). At increasing time delays from the discharge initiation the jet body gradually bends to the crossflow ( $3 < tU_\infty/D < 10$ ). Following the bending jet trajectory, an inclined propagation of the front vortex ring is experienced. The bending jet can be attracted to the pressure difference between the windward side and the leeward side of the jet body, as well as the horizontal acceleration imposed by the crossflow (Mahesh 2013).

Additional to the bending jet trajectory, a prominent flow phenomenon in the *xy* plane is the formation of recirculation region (defined by  $\overline{U_x} \leq 0$ ) residing in the leeward side of the jet body, as indicated by the solid black lines in Figure 6 (b)-(c). Similar to the separation region formed behind bluff bodies (Krajnovic & Davidson 2002), the recirculation region in the studied JICF is also accompanied by the production of unsteady vorticity, in the form of the so-called hanging vortices (Meyer, Pedersen & Oktayozcan 2007). The streamwise extent of the recirculation region is around  $1D$ , consistent with the observation in steady jets in crossflow (Gutmark, Ibrahim & Murugappan 2011). At  $tU_\infty/D=5$  ( $t=500 \mu s$ ) no clear vortex rings can be identified from the velocity fields, nevertheless the curved streamlines at the jet front indicate the residual concentration of vorticity. Additionally, the peak jet exit velocity drops significantly to  $2.4U_\infty$  (48m/s) at  $tU_\infty/D=5$  ( $t=500 \mu s$ ). From  $tU_\infty/D=10$  ( $t=1000 \mu s$ ) on, the jet effectively terminates and the velocity fields in Figure 6 (d)-(f) show similar patterns. The issued jet body is severed from the orifice and experiences a quasi-drifting motion along the streamwise direction. During this drifting motion, momentum of the jet flow is gradually dissipated as a result of the mixing with turbulent crossflow.

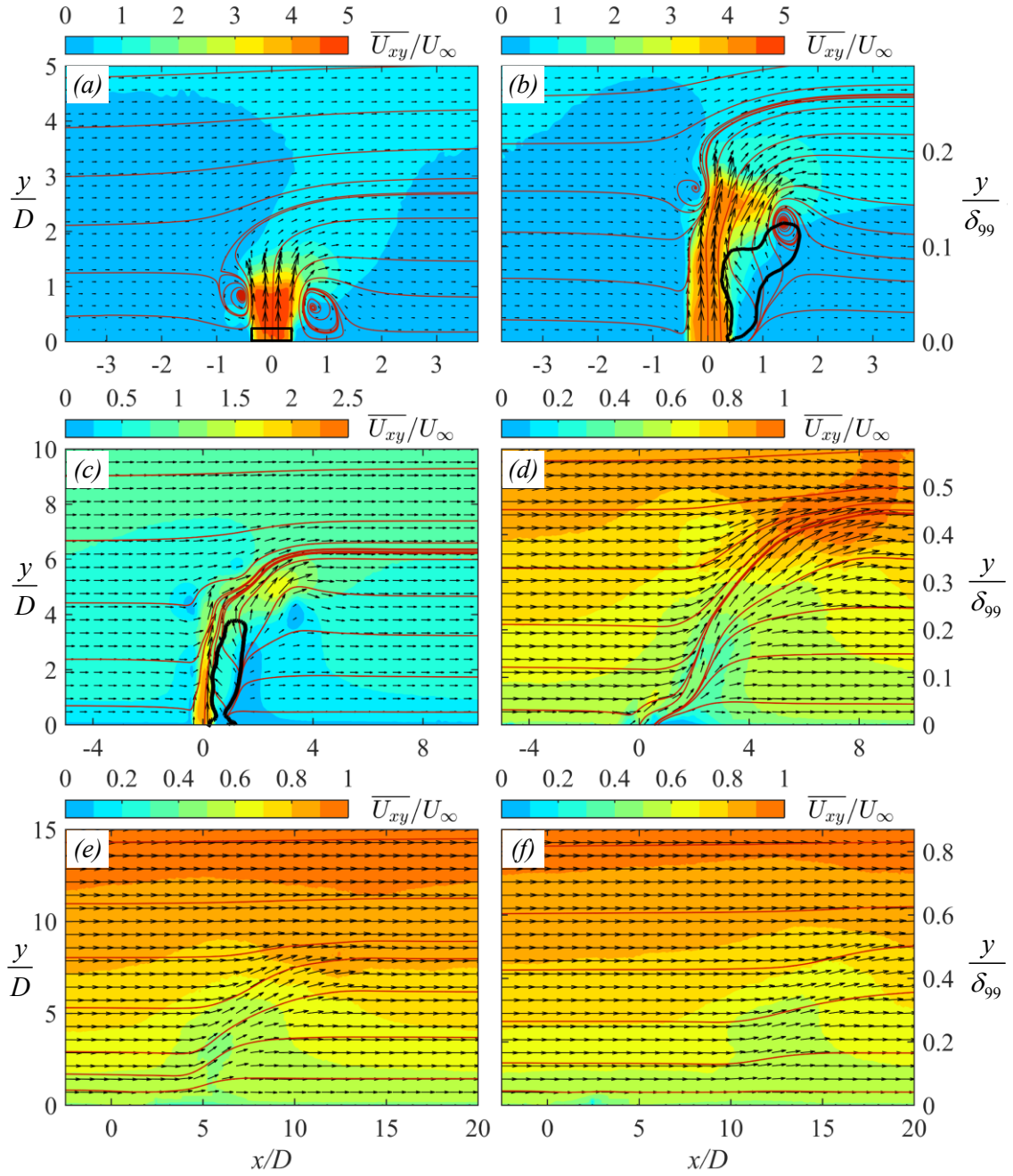


FIGURE 6. Phase-averaged velocity fields in the  $xy$  plane ( $z=0$  mm). (a)  $tU_\infty/D=2$  ( $t=200\mu s$ ), (b)  $tU_\infty/D=3$  ( $t=300\mu s$ ), (c)  $tU_\infty/D=5$  ( $t=500\mu s$ ), (d)  $tU_\infty/D=10$  ( $t=1000\mu s$ ), (e)  $tU_\infty/D=15$  ( $t=1500\mu s$ ) and (f)  $tU_\infty/D=25$  ( $t=2500\mu s$ ). Note that both the spatial scales and colourmap ranges are changing. The red lines superimposed on contour are phase-averaged streamlines. The recirculation regions at  $tU_\infty/D=3$  and  $tU_\infty/D=5$  (defined by  $\overline{U}_x \leq 0$ ) are indicated by solid black lines. The interrogation window used to obtain the jet exit velocity is illustrated in Figure 6 (a) by a solid black rectangle.

The area of the recirculation region ( $A_r$ ) is computed, as shown in Figure 7. After each actuation pulse, the recirculation region increases in size prior to  $tU_\infty/D=5$  ( $t=500\mu s$ ), shrinks afterwards and disappears completely after  $tU_\infty/D=10$  ( $t=1000\mu s$ ). The peak value of  $A_r$  is just over three times of the exit orifice area ( $A_e$ ). This agrees qualitatively with the results reported in steady jets in crossflow,

where a nondimensional area of 2 is observed for a velocity ratio of 3 (Gutmark, Ibrahim & Murugappan 2011). The increase of  $A_r$  in Figure 7 is ascribed to the continuing penetration of the high-speed jet body, while the decrease is directly related to the drop of jet exit velocity since the blocking effect diminishes considerably. With a velocity ratio as low as 0.17, no clear jet body and recirculation region can be observed and a train of hairpin vortices will emanate consecutively from the exit orifice (Wen & Tang 2014).

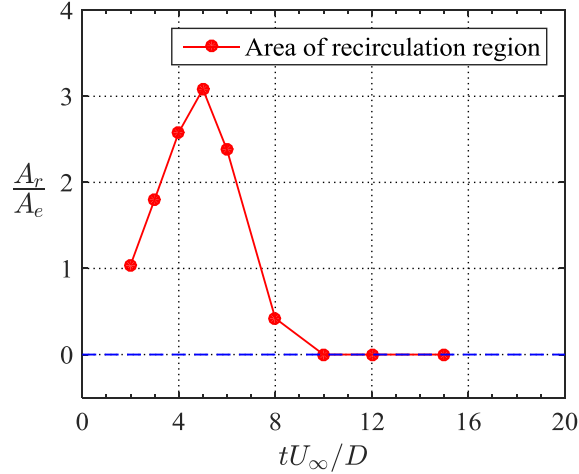


FIGURE 7. Area of the recirculation region as a function of the nondimensional time

The temporal evolution of the phase-averaged jet exit velocity can be monitored using an interrogation window located just above the jet exit (Zong & Kotsonis 2016a). The used interrogation window is indicated in Figure 6 (a) by a solid black rectangle. The exit velocity values reported in Figure 8 are the spatially-averaged values in the interrogation window. The two components of the jet exit velocity in  $x$  and  $y$  direction are denoted as  $\overline{U_{ex}}$  and  $\overline{U_{ey}}$  respectively. The variation of  $\overline{U_{ex}}$  and  $\overline{U_{ey}}$  in crossflow is plotted in Figure 8 as a function of the nondimensional convective time units. For comparison, the experimental data for  $\overline{U_{ey}}$  in the quiescent flow for an identical actuator are also shown (excerpted from Zong & Kotsonis 2016b)).

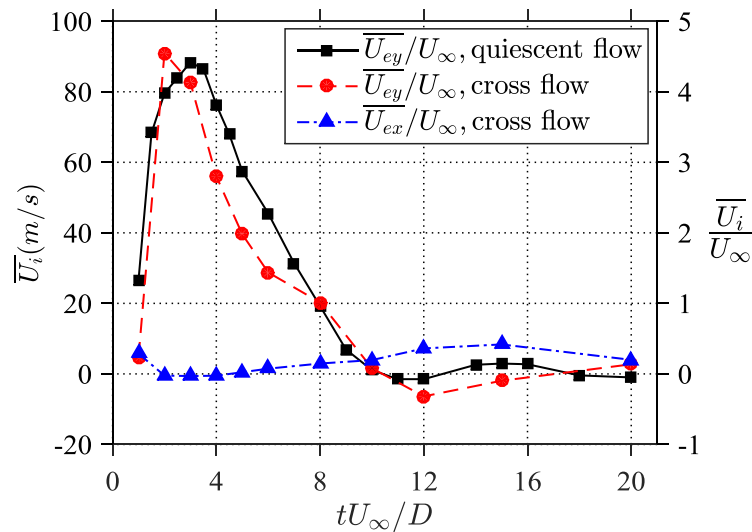


FIGURE 8. Exit velocity variation with the non-dimension time in both quiescent and cross flow conditions.

After each actuation pulse,  $\overline{U_{ey}}$  initially shows a sharp increase and then a slow decrease. In both cases, the peak values of  $\overline{U_{ey}}$  are around  $4.5U_\infty$  (90 m/s). After  $tU_\infty/D=10$  ( $t=1000 \mu s$ ), a small negative exit velocity is evident, indicating the start of the refresh stage of the actuator. The peak suction velocity in the refresh stage is approximately  $-0.3U_\infty$  (-6 m/s), considerably lower than the peak jet velocity. This feature promotes the conclusion that as a typical synthetic jet actuator, PSJA has an inherent zero-net mass flux whereas nonzero-net momentum flux. As a result, a quasi-steady impulse (net impulse) will be produced by PSJA working in repetitive mode, with promising extensions towards flight control (Anderson & Knight 2012). Based on the sign change of  $\overline{U_{ey}}$ , the nondimensional jet duration time (denoted as  $T_{jet}U_\infty/D$ ) is determined to be 10 ( $T_{jet}=1000 \mu s$ ) in both crossflow and quiescent conditions. Overall, the two curves of  $\overline{U_{ey}}$  agree well, although some disparities exist between  $tU_\infty/D=3$  and  $tU_\infty/D=8$ . This agreement is largely expected, as suggested by the analytical model proposed by Zong et al. (2015) where only significant changes in external atmospheric parameters (ambient pressure, temperature and density) can alter the exit velocity variation of PSJA. Thus, for the investigated case the external flow condition has little influence on the variation of the jet exit velocity. Additionally, a nonzero lateral component of the jet exit velocity is exhibited in crossflow.  $\overline{U_{ex}}$  varies inversely with  $\overline{U_{ey}}$ , with a peak value of  $0.5U_\infty$  (10 m/s).

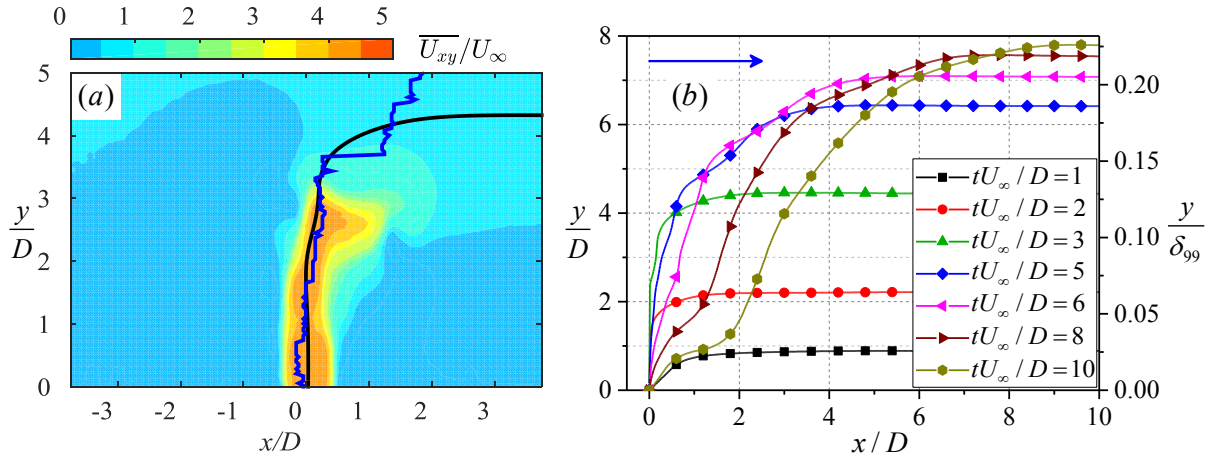


FIGURE 9. (a) Comparison of jet trajectories at  $tU_\infty/D=3$  ( $t=300 \mu s$ ) extracted from the positions of local velocity maxima (blue line) and the jet exit centre streamline (black line). (b) Temporal evolution of the phase-averaged streamlines originating from the jet exit centre.

In order to quantify the penetration ability of the PSJA, the jet trajectories at different time delays are evaluated. For steady jets in crossflow, the jet trajectory can be defined as the positions of local velocity maxima (Kamotani & Greber 1972), local vorticity maxima or as the ensemble-averaged streamline originating from the jet exit centre (Mahesh 2013). For PSJ in crossflow, the vorticity prior to  $tU_\infty/D=5$  ( $t=500 \mu s$ ) is largely concentrated in the front vortex ring. Thus the vorticity criterion cannot be deployed. Comparison of the other two criteria is made in Figure 9 (a). As evidenced, the jet trajectory defined by the phase-averaged streamline is more robust, thus suitable for this study.

The temporal evolution of the jet trajectories is shown in Figure 9 (b). For each streamline, there exists an asymptotic plateau. The  $y$ -coordinate of this plateau reflects the phase-averaged jet penetration depth, which increases monotonically with nondimensional time. In contrast to steady jets (Yuan & Street 1998), the jet trajectories of PSJ exhibit noticeable inflection points after  $tU_\infty/D=3$  ( $t=300 \mu s$ ). This phenomenon is attributed to the dynamic change of the jet exit velocity within an actuation cycle. Specifically, the ability of the jet body to resist the crossflow diminishes significantly with time, leading to an increased curvature of the jet trajectories and finally the formation of inflection points.

Between  $tU_\infty/D=3$  and  $tU_\infty/D=10$ , a considerable downstream drift of the jet body is evidenced by the streamwise offsets between the observed jet trajectories. After  $tU_\infty/D=10$  ( $t=1000 \mu s$ ), the PSJA enters the refresh stage. In this stage, a stagnation point is formed just above the exit, separating the preceding ejection and the anticipating suction flow (Glezer & Amitay 2002, Zong & Kotsonis 2016a). Affected by this stagnation point, the streamline originating from the jet exit centre no longer represents the actual jet trajectory. An alternative method will be introduced at a later point to quantify the jet penetration during the refresh stage.

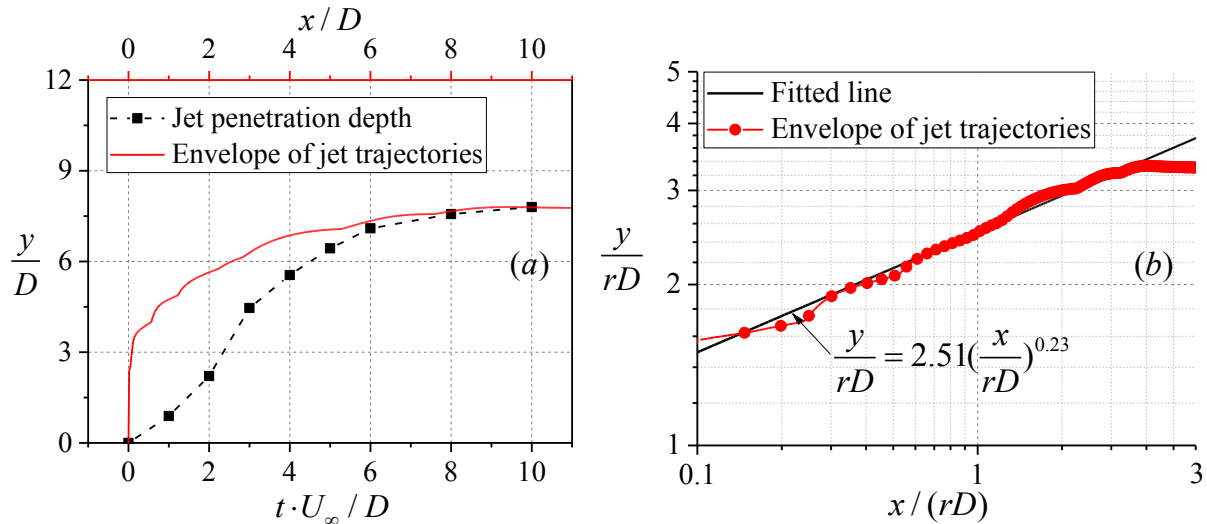


FIGURE 10. (a) Outer envelope of the jet trajectories and temporal variation of the jet penetration depth. (b) Jet trajectory envelope in double logarithmic coordinate. The formula of the fitted line is indicated.

The outer spatial envelope of the jet trajectories in Figure 9(b) is extracted and shown in Figure 10(a). Below this envelope lies the region possibly swept by the PSJ. In addition, the variation of the jet penetration depth, defined as the  $y$ -coordinate of the plateau in Figure 9 (b), is shown in Figure 10 (a) as a function of the nondimensional time  $tU_\infty/D$ .  $tU_\infty$  can be interpreted as the maximum convective distance of the jet core in the crossflow. Thus, at any time of the jet stage ( $tU_\infty/D < 10$ ), the jet front should fall into the enclosed region defined in Figure 10 (a). The peak value of the jet penetration depth within the jet stage is estimated to be  $7.8 D$  ( $0.45\delta_{99}$ ).

The pronounced similarity between the jet trajectory envelope of the PSJ and the previously studied jet trajectory of steady jets allows a comparison of their penetration ability. Jet trajectories are

most commonly scaled with  $rD$  (Smith & Mungal 1998), where  $r$  is defined as the ratio of the *momentum flow velocity* ( $U_m$ ) to the freestream velocity as shown in Equation (2). The momentum flow velocity here ( $U_m$ ) as expressed explicitly in Equation (2) shares a similar definition with that in Cater & Soria (2002), which is based on the equivalent integral of velocity square in the jet stage.

$$\begin{cases} r = \frac{U_m}{U_\infty} \\ U_m = \sqrt{\frac{1}{T_{jet}} \int_0^{T_{jet}} \overline{U_{ey}}(t)^2 dt} \end{cases} \quad (2)$$

For the investigated case,  $U_m$  and  $r$  are calculated to be 46.8m/s and 2.34 respectively. In Figure 10(b), the normalized jet trajectory envelope is plotted in a double logarithmic coordinate, and an approximate linear variation is exhibited in  $x/(rD) < 2$ . This suggests that the jet trajectory envelope of PSJ can also be fitted by the following equation (Margason 1993)

$$\frac{y}{rD} = A \left( \frac{x}{rD} \right)^B \quad (3)$$

where,  $A$  and  $B$  are coefficients to be determined. For steady jets in crossflow, Margason (1993) summarized the possible ranges of  $1.2 < A < 2.6$  and  $0.28 < B < 0.34$ . In the current case of PSJ in crossflow, the fitted value of  $B$  (0.23) is beyond that range, indicating the penetration ability of PSJ is not as strong as steady jets with the same momentum flow velocity. When  $rD$  is fixed, increasing the jet duration time ( $T_{jet}$ ) is expected to enhance the penetration ability of PSJ.

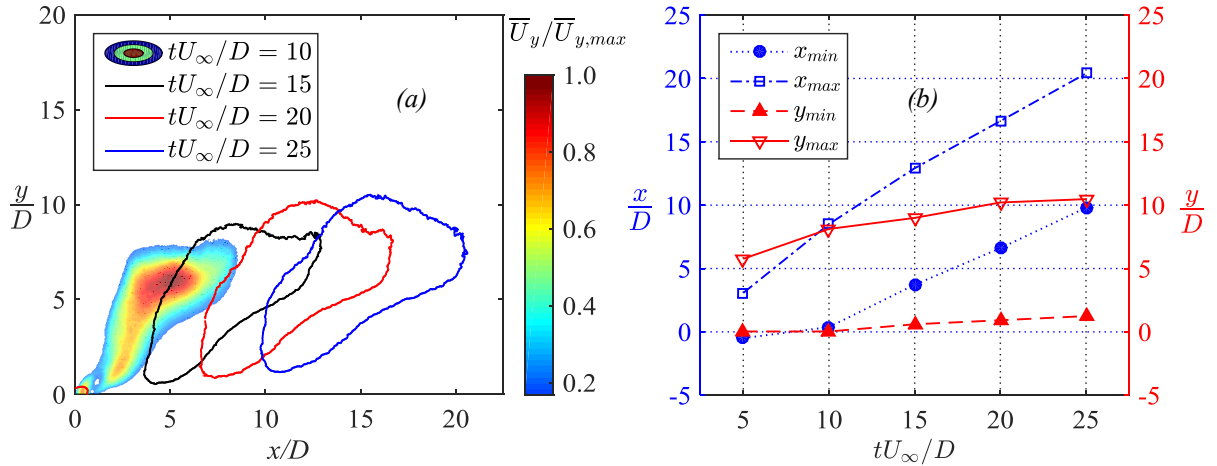


FIGURE 11 (a). Projection of the jet body outlines in the  $xy$  plane determined by the contour of 20% of the maximum wall-normal velocity ( $\overline{U}_{y,max}$ ). (b) Streamwise and wall-normal bounds of the jet body outlines in the  $xy$  plane.

The above analysis is performed based on the jet trajectories during the jet stage. As mentioned previously, after  $tU_\infty/D=10$  ( $t=1000 \mu s$ ) an alternative method should be proposed to track the motion of the jet body. In the  $xy$  plane ( $z=0$  mm), the jet body convects downstream and away from the wall after the jet issuing is terminated, thus the region with large  $\overline{U}_y$  can represent the projection of the jet body in the  $xy$  plane to some extent. In this study, a threshold value of 20% of the maximum wall-

normal velocity (denoted as  $\overline{U}_{y,\max}$ ) is exploited to extract a well-defined outline of the jet body in the  $xy$  plane (Gutmark, Ibrahim & Murugappan 2011), as shown in Figure 11 (a).

While convecting downstream, the jet outline in the  $xy$  plane remains largely similar. The streamwise bounds ( $x_{\min}, x_{\max}$ ) and wall-normal bounds ( $y_{\min}, y_{\max}$ ) of the extracted outlines are plotted in Figure 11 (b) as a function of the convective time scale. The linear variation of  $x_{\max}$  indicates an approximately unchanged convection velocity of the jet body (mean value:  $0.85U_\infty$ ).  $x_{\max}-x_{\min}$  defines the occupied streamwise extent of the jet body ( $L_{x0}$ ). In principle,  $L_{x0}$  increases with nondimensional time, due to the significant velocity gradient in  $y$ -direction. At  $tU_\infty/D=25$  ( $t=2500 \mu s$ ),  $L_{x0}$  is about  $10D$ .  $y_{\max}$  can be interpreted as the jet penetration depth of the PSJ. As expected,  $y_{\max}$  experiences a monotonic increase and reaches a peak value of  $10 D$  ( $0.58 \delta_{99}$ ) at  $tU_\infty/D=25$  ( $t=2500 \mu s$ ). From this point of view, the PSJA used in this study still fits in the category of sub-boundary-layer vortex generators (Ashill, Fulker & Hackett 2002), although a peak velocity ratio of 4.6 is reported.

#### 4.2 $yz$ plane

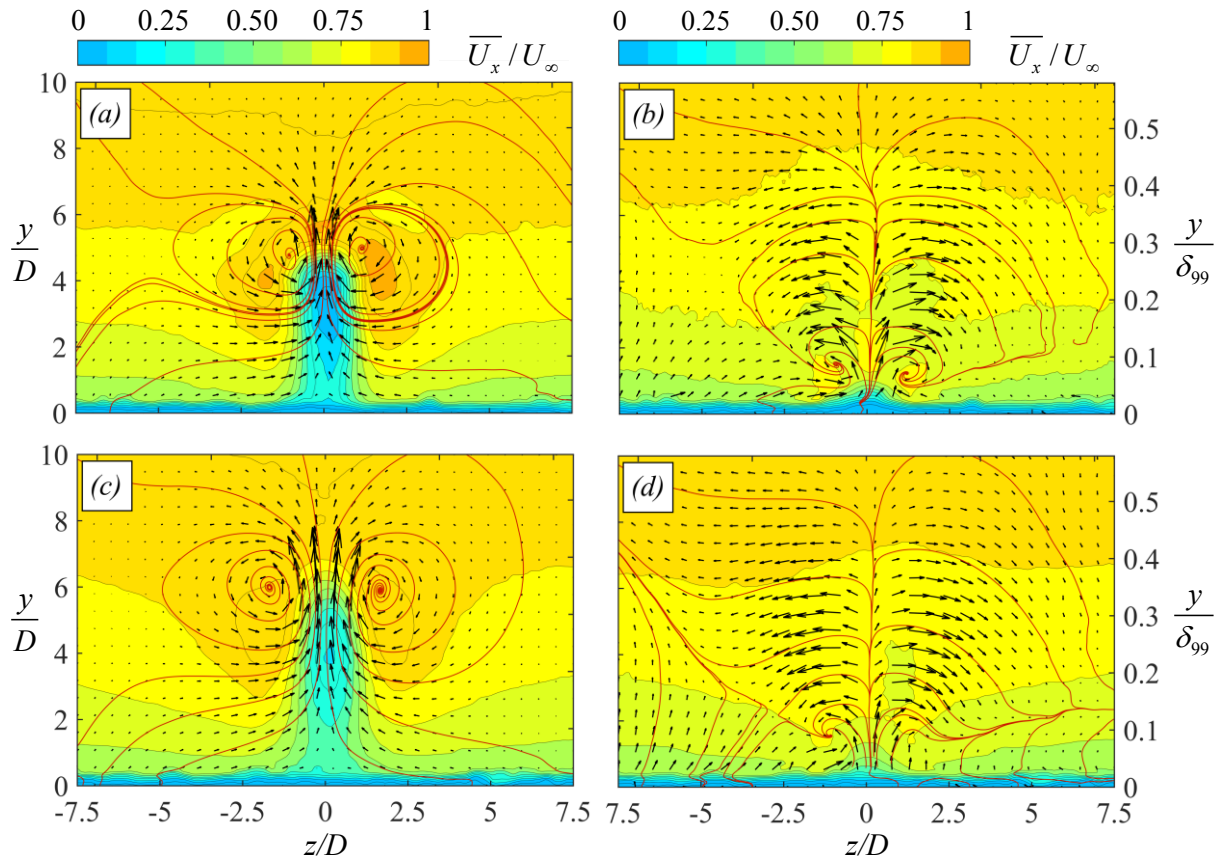


FIGURE 12. Representative velocity fields in the  $yz$  plane. (a)  $tU_\infty/D=5$  ( $t=500\mu s$ ),  $x/D=2.5$ ; (b)  $tU_\infty/D=10$  ( $t=1000\mu s$ ),  $x/D=2.5$ ; (c)  $tU_\infty/D=10$  ( $t=1000\mu s$ ),  $x/D=5$ ; (d)  $tU_\infty/D=15$  ( $t=1500\mu s$ ),  $x/D=5$ ; The out-of-plane velocity component ( $\overline{U}_x$ ) is plotted as contours, while the in-plane velocity components ( $\overline{U}_y$  and  $\overline{U}_z$ ) are shown by black vectors and red streamlines.

Due to the convective nature of the emitted jet, several appropriate time delays are selected to perform the stereo-PIV measurement for each of the five  $yz$  planes listed in Table 1. The captured flow

fields exhibit two distinct topologies. For each topology, two representative samples are shown in Figure 12. In Figure 12 (a) and (c), a prominent counter-rotating vortex pair (CVP) is observed, similar to that perceived in steady jets in crossflow (Kamotani & Greber 1972). Driven by the CVP, the low-momentum flow in the near-wall region is ejected upward while the high-momentum flow in the outer layer is swept downward, as indicated by the contour lines of  $\overline{U}_x$ . The origin of the CVP is still a debated topic in JICF-related literature. Marzouk & Ghoniem (2007) suggest that the stretch and deformation of the jet shear layer vortices initiate the CVP. However, Meyer, Pedersen & Oktayozcan (2007) argue that the hanging vortices may be the origin of the CVP and contribute a significant part of the vorticity to the CVP. While the origin of the CVP is beyond the scope of the current work, the available planar and stereo PIV measurements can only offer inconclusive conjectures on this issue, and as such will not be currently considered.

Figure 12 (b) and Figure 12 (d) correspond to the second topological structure. In this topology, the CVP is not well-defined, although the streamlines are severely curled at  $z/D=\pm 1$ ,  $y/D=1.5$ . A positive bifurcation line is observed around  $z/D=0$ , separating the velocity vectors with opposite  $z$ -component (Kelso, Lim & Perry 1996). This flow scenario seems to be a plane projection of a second highly inclined counter-rotating vortex pair—possibly the so-called hanging vortex pair observed by Yuan, Street & Ferziger (1999). The hanging vortex pair is a quasi-steady structure residing at the sides of the jet. In the near-wall region, its axis is highly inclined and interacts with the wall. However, at higher values of  $y$ , it behaves unpredictably and possibly contributes vorticity to the CVP (Yuan, Street & Ferziger 1999). Its formation is closely related to the skewed mixing layer on the sides of the jet (Kelso et al. 1996). In the same streamwise location, the second flow topology appears 500  $\mu\text{s}$  (5 convective time units) after the occurrence of the first topology.

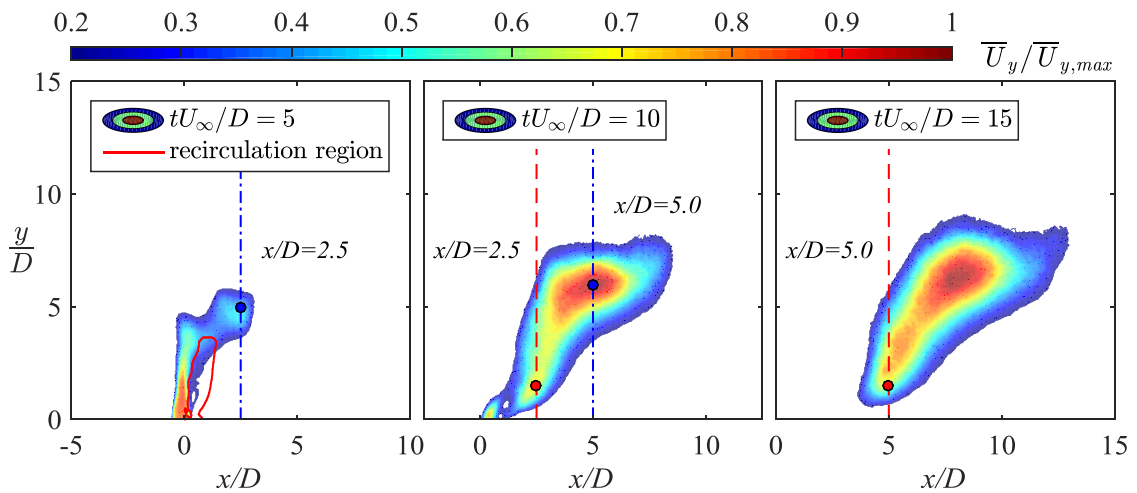


FIGURE 13. Relationship between the resolved flow topology and the streamwise measurement locations. The four vertical lines indicate the streamwise measurement locations of the four cases shown in Figure 12. The first and the second flow topology are denoted by blue dash-dot lines and red dash lines respectively. The vortex center locations determined roughly from the streamlines in Figure 12 are indicated by the solid points.

The measurement planes pertaining to the four cases in Figure 12 are further illustrated in Figure 13 in the  $xy$  plane ( $z=0$  mm). Due to the upwash effect, the CVP can be visualized by the region with high  $\overline{U}_y$  (the case of  $tU_\infty/D=5$  is not included, as the high value of  $\overline{U}_y$  is directly associated with the high-speed jet, instead of the CVP). All the measurement planes presented in Figure 12 intersect the jet body. Judging from the spatial distribution of high  $\overline{U}_y$ , the aforementioned hanging vortex pair seems to be connected with the CVP. Both of them bear a curved shape, following the jet outline. This conjecture is consistent with the perspective of Meyer, Pedersen & Oktayozcan (2007) that the hanging vortices transport a significant part of the vorticity into the CVP. The two distinct flow topologies observed earlier can be ascribed to the different intersection angles between the CVP axis and the PIV measurement plane. At the jet front, the CVP bends largely to the crossflow, and thus can be well-depicted by the stereo-PIV results (Figure 12 (a) and (c)) in the  $yz$  plane. In contrast, with a measurement plane intersecting the ‘root’ of the jet outline (Figure 12 (b) and (d)), only the induced wake flow of the hanging vortex pair will be resolved.

In contrast to steady jets in crossflow, the CVP produced by the PSJ in crossflow exhibits a strongly dynamic spatiotemporal behaviour. Due to the short jet duration time, the CVP occupies a rather limited streamwise extent which can be approximated by  $L_{x0}$  ( $10D$ ). In addition, the CVP bears steady streamwise convection during the evolution. Thus, the residence time of the CVP (denoted as  $T_{CVP}$ ) in a specific streamwise location is also finite and can be estimated by the jet duration time ( $1000 \mu\text{s}$ ). From this point of view, the actuation imposed by PSJ is inherently intermittent due to the essential alternation between the jet stage (ejection) and the refresh stage (suction) (Zong et al. 2015).

The following analysis aims at quantifying the intensity of the CVP from two aspects: the total circulation ( $\Gamma_{CVP}(x,t)$ ) and the variation of the TBL shape factor ( $H(x,z,t)$ ). According to the results shown in Zong & Kotsonis (2016b), the peak relative difference between the jet exit density and the ambient density is less than 8% for the current investigated cases. This observation, in conjunction with a peak jet velocity of less than Mach 0.3 fully justifies the assumption of incompressible flow. The boundary layer shape factor in incompressible flow is defined as follows (Schlichting, 1979).

$$H(x,z,t) = \frac{\delta^*}{\theta} = \frac{\int_0^\infty (1 - \frac{\overline{U}_x}{U_\infty}) dy}{\int_0^\infty \frac{\overline{U}_x}{U_\infty} (1 - \frac{\overline{U}_x}{U_\infty}) dy} \quad (4)$$

where,  $\delta^*$  and  $\theta$  denote the displacement thickness and the momentum thickness respectively. Based on the phase-averaged stereo-PIV results, the shape factor at different spanwise and streamwise locations is computed, as shown in Figure 14 (a). In addition, the boundary layer profiles corresponding to the streamwise locations and time delays of Figure 14 (a) are shown in Figure 14 (b) for several spanwise locations. The shape factor (1.3) and velocity profiles pertaining to the baseline case (no jet) are indicated as reference.

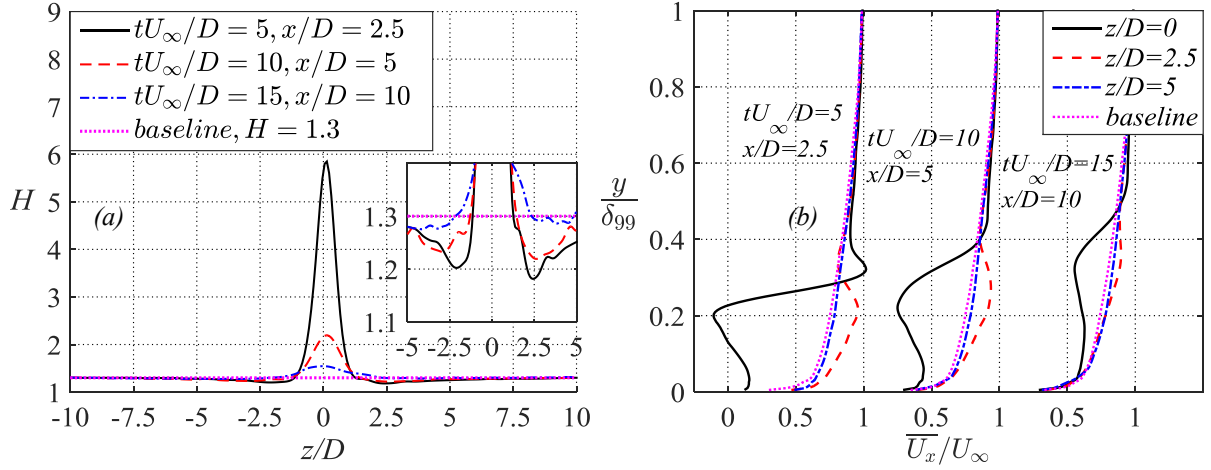


FIGURE 14. (a) Spanwise distribution of the boundary layer shape factor. A zoomed view of the variation is shown in the inset. (b) Boundary layer velocity profiles. The corresponding streamwise measurement stations and time delays are indicated by the annotations. Note that the  $x$  axis changes repetitively from 0 to 1.

The spanwise distribution of  $H$  assumes the form of a Mexican hat function, where a large positive peak is observed in the middle ( $z/D=0$ ) surrounded by two negative peaks. For the case of  $tU_\infty/D=5$  ( $t=500\mu s$ ),  $x/D=2.5$ , the positive peak of  $H$  is extremely high, reaching 5.85. This can be attributed to the recirculation region situated at the leeward side of the jet body, which creates a large velocity deficit in  $y < 0.3\delta_{99}$  at  $z/D=0$  (Figure 6). The downwash effect of the CVP is most prominent at  $z/D=\pm 2.5$ , where two negative peaks of  $H$  (approximately 1.2) are evident and the corresponding velocity profile becomes relatively fuller. Specifically, an accelerated region is formed below  $y=0.3\delta_{99}$ , due to the continuous transport of the high-momentum flow from the outer layer to the near-wall region. As a result, the TBL is energized, and expected to have an enhanced ability to resist streamwise adverse pressure gradients. (Johnston & Nishi 1990)

As the CVP propagates downstream, both the deficit region and the accelerated region move away from the wall. Meanwhile, the actuated velocity profiles gradually recovery to the baseline shape, suggesting a weakened intensity of the CVP. The velocity profiles at  $z/D=\pm 5$  for all cases show little difference with the baseline cases. Therefore, the effective extent of the CVP in the spanwise direction is determined to be approximately  $10 D$ . Compared to the results of conventional synthetic jets in crossflow (Smith 2002), the results reported here are considerably positive. Smith (2002) experimentally investigated the interaction between a piezoelectric synthetic jet array (three actuators, rectangle orifices, wall-normal jet) with a TBL. The ratio of the time-averaged jet velocity (11.3 m/s) to the freestream velocity (9.1 m/s) was 1.2. Considering a sinusoidal variation of the instantaneous jet velocity, the peak velocity ratio (not reported) is estimated to be around 3.8, comparable to the present case (4.6). The boundary layer shape factors were examined in a large streamwise and spanwise extent. As a result, no obvious decrease of the boundary layer shape factor was observed. However, a distinction should be made concerning the fact that the results from Smith (2002) are time-averaged, while in the present study are phase-averaged.

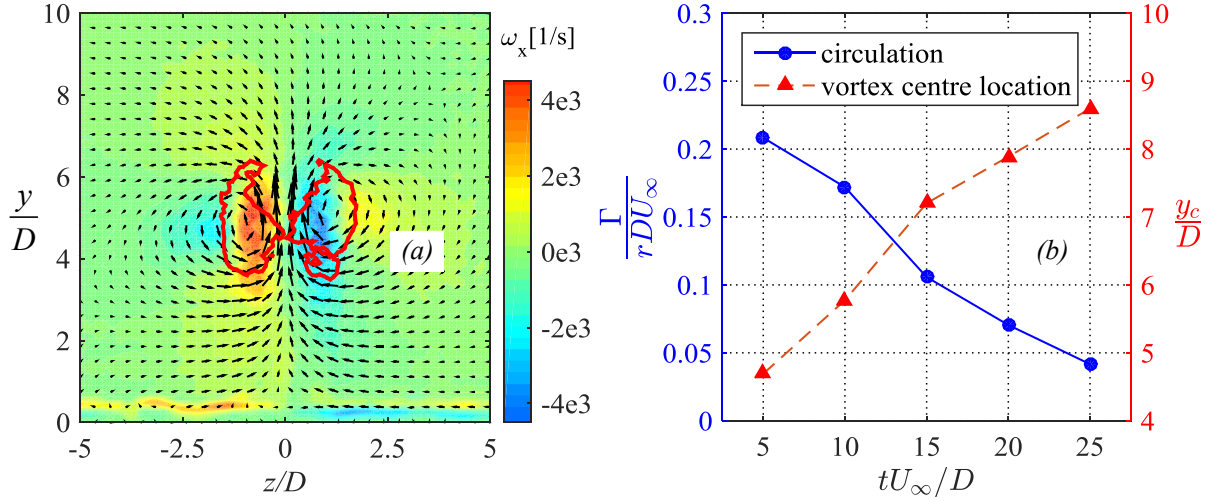


FIGURE 15. (a) Streamwise vorticity field superimposed with in-plane velocity vectors at  $x/D=2.5$ ,  $tU_\infty/D=5$ . The vortex regions identified by the Q-criterion are indicated by the red lines. (b) Temporal evolution of the total circulation and the wall-normal location. It should be noted that the five data points are acquired at different streamwise stations ( $x/D=2.5, 5, 10, 15$  and  $20$ ).

The following analysis concerns the characteristics of the CVP. A representative vorticity field in the  $yz$  plane ( $x/D=2.5$ ,  $tU_\infty/D=5$ ) is shown in Figure 15 (a). High vorticity mainly resides in the CVP cores and the near-wall region. To identify the CVP from the background, Q-criterion is used and the threshold value is chosen as 1% of the peak Q-value. The identified vortex regions are outlined by red lines in the vorticity contour. The total circulation ( $\Gamma$ ) and the wall-normal location ( $y_c$ ) of the CVP are defined as follows.

$$\begin{cases} \Gamma = \frac{1}{2} \iint_{\Omega} |\omega_x| dydz \\ y_c = \frac{1}{2\Gamma} \iint_{\Omega} y |\omega_x| dydz \end{cases} \quad (5)$$

where  $\Omega$  denotes the identified vortex region. A preliminary sensitivity study shows that when the threshold reduces to 0.1% of the peak Q-value, a small portion of the near-wall shear-layer region will be included as the vortex region. Nevertheless, the relative variation in  $\Gamma$  and  $y_c$  is less than 7%.

The variations of  $\Gamma$  and  $y_c$  are shown in Figure 15 (b) as a function of the nondimensional time ( $tU_\infty/D$ ). Since the spanwise spacing and the peak vorticity of the CVP are expected to scale with  $D$  and  $rU_\infty/D$  respectively, the total circulation ( $\Gamma$ ) can be reasonably normalized by  $rDU_\infty$ . The nondimensional total circulation  $\Gamma/(rDU_\infty)$  is on the order of 0.1, and appears decreasing approximately linearly with the nondimensional time. At  $tU_\infty/D=25$  ( $t=2500\mu s$ ), the total circulation remains only 20% of that at  $tU_\infty/D=5$  ( $t=500\mu s$ ). By extrapolation, the nondimensional survival time of the CVP is estimated to be 32. As stated earlier, this nondimensional time can be interpreted as the farthest propagation distance of the jet body. Thus, the maximum effecting extent of the CVP in  $x$ -direction is also  $32D$ . Beyond this extent, the total circulation will drop to a negligible level. In addition,  $y_c$  increases monotonically with the nondimensional time, indicating a lift motion of the CVP. This self-induced lift motion is a common behaviour of the vortex pair/ vortex ring formed at

orifice openings (Pullin 1979). In principle, the lifting velocity is positively proportional to the ratio of the total circulation to the vortex ring diameter (Wu, Ma & Zhou 2007). As  $\Gamma$  drops, the rising rate of  $y_c$  declines. The peak value of  $y_c$  at  $tU_\infty/D=25$  ( $t=2500\mu s$ ) is just above  $8.5D$ .

Based on the previous analysis, the spatiotemporal characteristics of the CVP are summarized. The CVP bears a convective motion with the crossflow, meanwhile lifting slowly. The residence time at a specific streamwise location is estimated to be the jet duration time ( $T_{jet}$ ). The maximum effecting extent of the CVP in the three coordinate directions ( $x$ ,  $y$  and  $z$ ) is approximately  $32D$ ,  $8.5D$  and  $10D$ , respectively.

## 5. Turbulent kinetic energy (TKE)

### 5.1 $xy$ plane

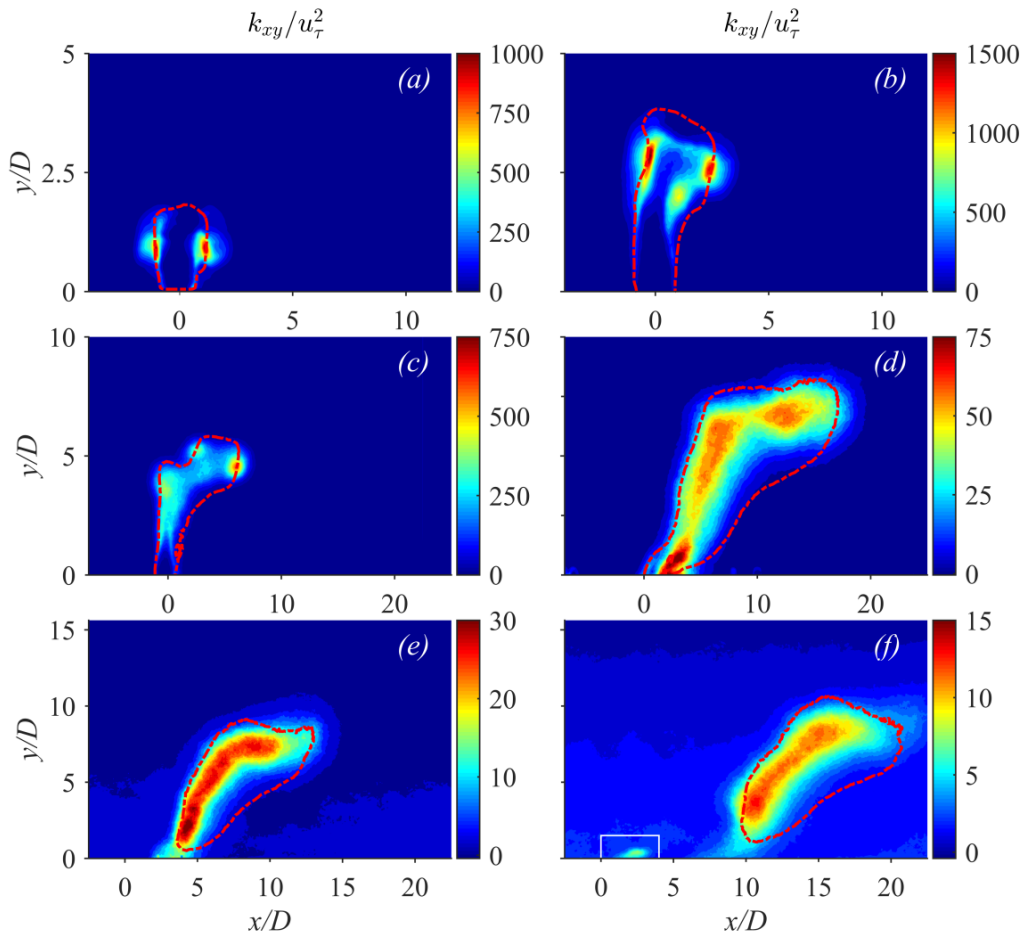


FIGURE 16. Contours of  $k_{xy} / u_\tau^2$  at different time delays. (a)  $tU_\infty/D=2$  ( $t=200\mu s$ ), (b)  $tU_\infty/D=3$  ( $t=300\mu s$ ), (c)  $tU_\infty/D=5$  ( $t=500\mu s$ ), (d)  $tU_\infty/D=10$  ( $t=1000\mu s$ ), (e)  $tU_\infty/D=15$  ( $t=1500\mu s$ ) and (f)  $tU_\infty/D=25$  ( $t=2500\mu s$ ). Using the same criterion described in Section 4.1 (20% of  $\bar{U}_{y,max}$ ), the jet outlines are extracted and plotted as red dash-dot lines. The solid white rectangle in Figure 16(f) stands out an isolated high-TKE region caused by the second jet.

Since only two-component planar PIV measurements are performed in the  $xy$  plane ( $z=0$  mm), the TKE is computed using the relation of  $k_{xy} = 0.5(\overline{u_x^2} + \overline{u_y^2})$ . Contours of  $k_{xy} / u_\tau^2$  at different time delays are shown in Figure 16. The jet outlines extracted with the criterion of 20% of  $\bar{U}_{y,max}$  (see

*Section 4.1*) are plotted as red dash-dot lines for reference. Theoretically, the production rate of TKE can be expressed as  $P_k = -\overline{u_i u_j} \cdot \partial \overline{U_i} / \partial x_j$  (Schlichting 1979). Therefore, high TKE always resides in the region with high velocity gradient, namely the front vortex ring and the jet shear-layer. Additionally, the inevitable discharge timing uncertainty associated with pin-to-pin arc discharge can result in a fluctuation in the timing of the jet, and finally the production of pseudo-TKE. The magnitude of this pseudo-TKE can be estimated by  $\zeta^2 / u_\tau^2$ , where  $\zeta$  is the peak velocity fluctuation caused by discharge timing uncertainty (approximately 3 m/s, see Appendix). As a result, the peak pseudo-TKE is about  $14.4 u_\tau^2$ , significantly lower than the TKE value measured in the front vortex ring and jet shear-layer (Figure 16a and b). Thus, the influence of discharge timing uncertainty can be neglected during the following analysis. Prior to  $tU_\infty/D=5$  ( $t=500\mu s$ ), the TKE level in the jet shear-layer is lower than in the front vortex ring. The peak value of  $k_{xy}$  at  $tU_\infty/D=3$  ( $t=300\mu s$ ) is  $1500 u_\tau^2$ , significantly larger than that for the baseline case (no jet,  $4 u_\tau^2$ ). From  $tU_\infty/D=5$  ( $t=500\mu s$ ) to  $tU_\infty/D=10$  ( $t=1000\mu s$ ), the maxima of  $k_{xy}$  drops sharply from  $750 u_\tau^2$  to  $75 u_\tau^2$ , which can be attributed to the breakdown of the front vortex ring.

After  $tU_\infty/D=10$  ( $t=1000 \mu s$ ), the jet terminates and the high-TKE region is gradually transported downstream, following the general movement of the jet body (Figure 11). In Figure 16 (f), a localised area in the vicinity of the orifice (highlighted by the white solid line) is occupied by elevated TKE, which is attributed to the emission of a secondary jet. The existence of multiple jet stages in one working cycle was first predicated by the analytic model in Zong et al. (2015) and later validated by the PIV results in Zong & Kotsonis (2016a). The rather small area and short penetration depth suggest that the second jet has negligible influence on the crossflow.

### 5.2yz plane

In the  $yz$  measurement planes, stereo-PIV measurements provide access to all three velocity components, thus fully defining TKE by the relation of  $k = 0.5(\overline{u_x^2} + \overline{u_y^2} + \overline{u_z^2})$ . Contours of  $\overline{u_i^2}$  and  $k$  are shown in Figure 17. The wall-normal locations of the CVP determined in *Section 4.2* are superimposed as white circle points for reference. The four cases used here are consistent with those used in Figure 12. In Figure 17 (a) and (c), the high-TKE region takes a shape of double lobe. The wall-normal location of this lobe pair agrees well with that of the corresponding CVP. For different Reynolds normal stresses, the spatial distributions are quite similar yet the absolute values differ largely.  $\overline{u_x^2}$  contributes a significant part of the TKE, and  $\overline{u_y^2}$  closely follows. Compared with Figure 17 (a), the high-TKE region in Figure 17 (c) expands moderately while the peak value of  $k$  drops sharply, which can be ascribed to the fast entrainment of the low-energy flow. Figure 17 (b) and (d) correspond to the second flow topology shown in Figure 12 (b) and (d), where the measurement planes intersect the root of the CVP. In this case, the majority of the TKE remains to be contributed by  $\overline{u_x^2}$ . However, the spatial distributions of different Reynolds normal stresses exhibit a distinct difference. High  $\overline{u_x^2}$  is concentrated in the near-wall region, showing a triangle shape. High  $\overline{u_z^2}$  is also situated in the near-wall region whereas spreads more widely in the  $y$ -direction than  $\overline{u_x^2}$ . The distribution of  $\overline{u_y^2}$  takes a saddle shape, with two peaks observed at  $y/D=2.5$  and  $y/D=3.5$ .

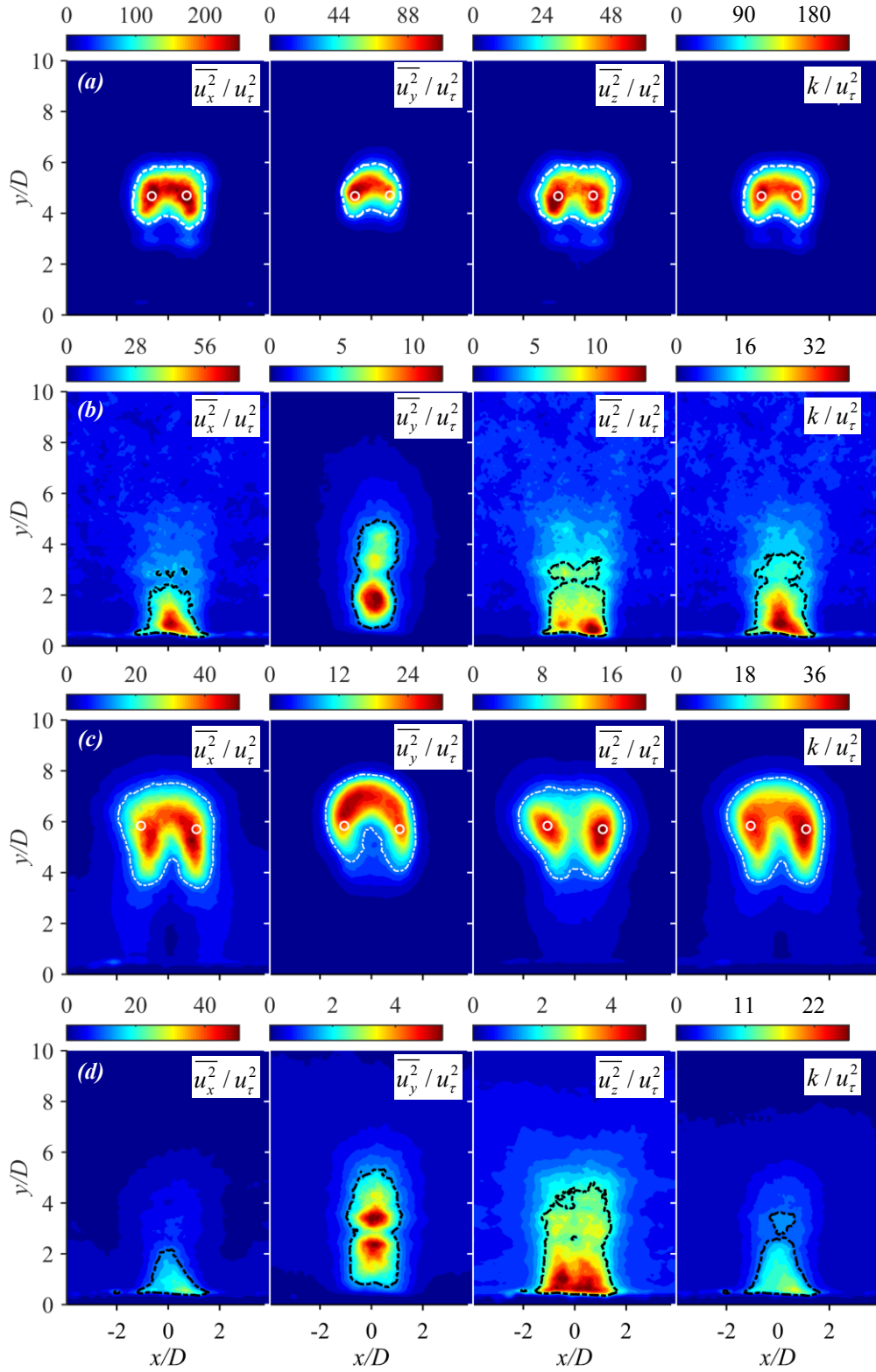


FIGURE 17. Contours of  $\overline{u_i^2}$  ( $i=x, y, z$ ) and  $k$  at the  $yz$  measurement planes. (a)  $tU_\infty/D=5$  ( $t=500\mu s$ ),  $x/D=2.5$ ; (b)  $tU_\infty/D=10$  ( $t=1000\mu s$ ),  $x/D=2.5$ ; (c)  $tU_\infty/D=10$  ( $t=1000\mu s$ ),  $x/D=5$ ; (d)  $tU_\infty/D=15$  ( $t=1500\mu s$ ),  $x/D=5$ ; The four cases here are consistent to the ones shown in Figure 12. The contour lines of 20% of the maxima are plotted as dash-dot lines for reference. The  $y$ -locations of the CVP determined in Section 4.2 are indicated by white circles.

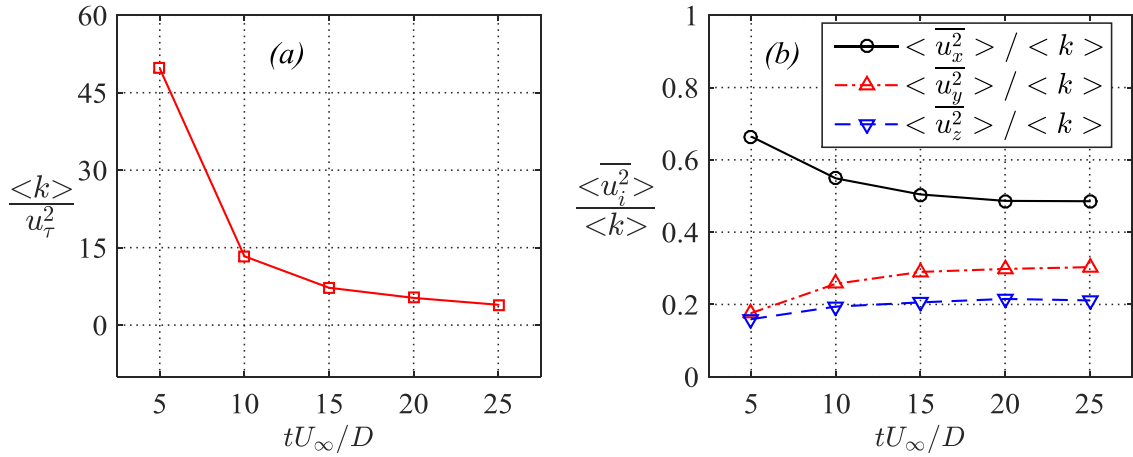


FIGURE 18. (a) Spatially-averaged TKE in the jet effecting region (defined by  $k / u_\tau^2 > 10$ ) as a function of the nondimensional time. (b) Contribution of different Reynolds normal stresses to the total TKE. It should be noted that the five data points at increasing time delays are collected at five different  $yz$  planes ( $x/D=2.5, 5, 10, 15$  and  $20$ ), same as that in Figure 15 (b).

In order to further analyse the contribution of each Reynolds normal stress to the total TKE, the spatially-averaged  $\overline{u_i^2}$  (denoted as  $\langle u_i^2 \rangle$ ) in the “jet effecting region” is calculated, and normalized by the spatially-averaged TKE (denoted as  $\langle k \rangle$ ). It should be noted that the jet effecting region here is defined by a criterion of  $k > 10 u_\tau^2$ , instead of the criterion used to extract the jet profiles in *Section 4.1* ( $\overline{U}_y > 0.2 \overline{U}_{y,\max}$ ). The evolution of  $\langle k \rangle / u_\tau^2$  and  $\langle u_i^2 \rangle / \langle k \rangle$  ( $i=x, y, z$ ) is shown in Figure 18 as a function of the nondimensional time.  $\overline{k}$  decreases rapidly with time. The contribution of  $\overline{u_x^2}$  to  $\overline{k}$  is always dominant. At  $tU_\infty/D=5$  ( $t=500\mu s$ ),  $\overline{u_x^2} / \overline{k}$  reaches the peak value of 66%. Afterwards, this ratio gradually decreases and finally keeps constant at about 0.5. For the contribution of  $\overline{u_y^2}$  and  $\overline{u_z^2}$ , their variation trends are opposite to that of  $\overline{u_x^2}$ . They grow slowly with time and reach the steady values (0.3 and 0.2 respectively) at about  $tU_\infty/D=20$  ( $t=2000\mu s$ ).

## 6. Conceptual model of PSJ in crossflow

A conceptual model of PSJ in crossflow is established based on the previous analysis as shown in Figure 19. Four time instants are selected, denoting four distinct stages of the evolution. It is beneficial to notice that this model doesn’t deny the existence of shear layer vortices, wake vortices and horseshoe vortices, since the measurements performed in this study are inconclusive regarding the origin of such structures.

At the first stage ( $tU_\infty/D=2$ ), a bulk of high-speed flow is rapidly released from a round orifice. Due to the short interaction time, a nominally erect jet body is exhibited, surrounded by a distinctive front vortex ring (see Figure 6 (a)). During the later interaction (second stage), the erect jet body gradually bends to the crossflow. Additionally, a recirculation region is observed in the leeward side of the jet body, associated with the hanging vortices (see Figure 6 (b-c)). A fraction of the flow in the

external crossflow is entrained into these hanging vortices, experiencing a spiral rising motion described by Meyer, Pedersen & Oktayozcan (2007).

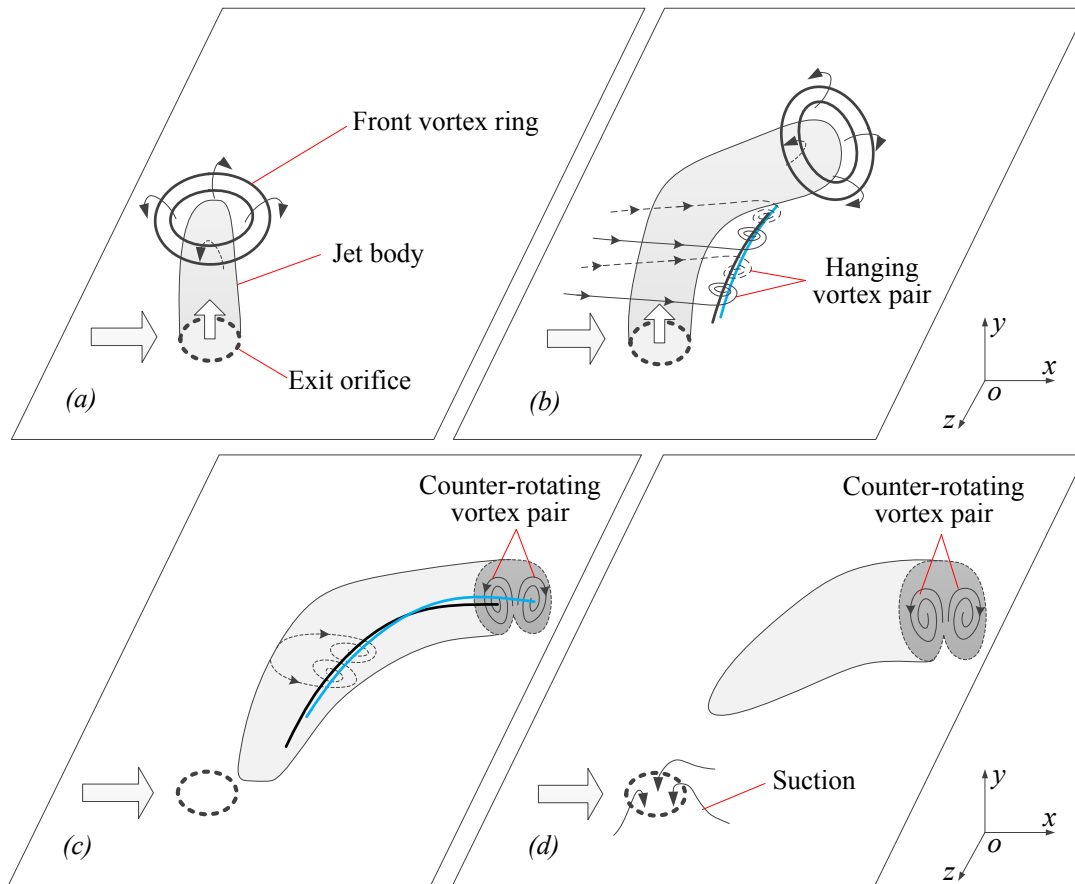


FIGURE 19. Conceptual model of PSJ in crossflow. (a) first stage ( $tU_\infty/D=2$ ); (b) second stage ( $tU_\infty/D=5$ ); (c) third stage ( $tU_\infty/D=10$ ); (d) fourth stage ( $tU_\infty/D=15$ ). Note that both the flow scenarios and their presenting time may change with the actuation parameters of PSJ.

At the third stage ( $tU_\infty/D=10$ ), the jet terminates and the front vortex ring disappears. The recirculation region no longer exists but the momentum deficit in the TBL velocity profile is still evident (see Figure 6 (d) & Figure 14 (b)). Note that the transition from the second to the third stage is not abrupt. The three major flow structures (front vortex ring, recirculation region and high-speed jet) don't need to diminish simultaneously. In addition, a quasi-streamwise-oriented CVP takes shape, which is ostensibly a natural extension of the aforementioned highly-inclined hanging vortex pair (see Figure 12-13). This CVP plays a significant role in enhancing the TBL's ability to resist a possible adverse pressure gradient. At the last stage, the PSJA steps into the refresh stage, ingesting the fresh near-exit flow into the cavity for recovery (see Figure 8). The CVP is detached from the wall, convecting downstream steadily while lifting up slowly (see Figure 11).

## 7. Conclusion

In this study, a three-electrode PSJA (cavity volume:  $1696 \text{ mm}^3$ , exit diameter: 2 mm) has been used to produce a high-speed pulsed jet (peak jet velocity: 92 m/s, jet duration time: 1 ms). The

interaction between this single-pulsed jet and a TBL (freestream velocity: 20 m/s,  $\delta_{99}$  thickness: 34.5 mm) under approximately zero pressure gradient is investigated with phase-locked PIV measurements. The phase-averaged flow organisation and the TKE distribution in both  $xy$  and  $yz$  measurement planes are analysed in detail.

For PSJA operated in crossflow, the exit velocity variation in one cycle remains almost identical to that operated in quiescent condition. However, the jet induced flow fields show abundant new features. In the  $xy$  plane ( $z=0$  mm), the initially issued erect jet body gradually bends to the crossflow and a time-dependent jet trajectory is exhibited. The peak penetration depth is just above  $10D$  ( $0.58\delta_{99}$ ). Comparison of the nondimensional jet trajectories suggests that the penetration ability of the PSJ is not as strong as the steady jets with the same momentum flow velocity. Prior to  $tU_\infty/D=10$  ( $t=1000 \mu s$ ), there exists a recirculation region in the leeward side of the jet body, experiencing an initial expansion and later contraction, with a peak area of three times of the exit orifice area.

In the  $yz$  plane, a signature vortical structure of JICF—CVP is observed. The downwash effect of the CVP transports the high-momentum fluids from the outer layer to the near-wall region, leading to a much fuller velocity profile and a decreased boundary layer shape factor between  $5D > z > -5D$ . The nondimensional total circulation of the CVP is on the order of 0.1, and decreases rapidly with the non-dimensional time. The maximum streamwise effecting extent of the CVP is determined to be  $32D$ , beyond which the total recirculation will drop to a negligible level. As the CVP drifts downstream, its wall-normal position increases as a result of the self-induction. The peak value of  $y_c$  is around  $8.5D$ .

In the  $xy$  plane, a considerably high level of TKE is shown at the front vortex ring and jet shear-layer. Prior to  $tU_\infty/D=10$  ( $t=1000\mu s$ ), the TKE level in the jet shear-layer is initially lower and afterwards equal to that in the front vortex ring. In the  $yz$  plane, the high-TKE region is closely associated with the CVP, taking a shape of double lobe. The spatially-averaged TKE in this double lobe ( $\bar{k}$ ) decreases exponentially with time, peaking at approximately  $50\bar{u}_t^2$ . Of the total TKE,  $\bar{u}_x^2$  constitutes the majority proportion while  $\bar{u}_y^2$  follows.

To summarize, the influence of single PSJA on the TBL is significant in the sense of velocity profile change and TKE production, yet short-lived in time domain and locally-confined in space domain. In future work, the interaction between a PSJA array working in repetitive mode and a crossflow TBL should be investigated. The spatiotemporal scales obtained in this paper provide useful instructions in the optimal design of PSJA arrays.

## Appendix: PIV Measurement Uncertainty

Finite sample size, peak locking error, limited spatial resolution, finite laser sheet thickness and discharge timing uncertainty are identified as the five main sources of PIV measurement uncertainty in the present study. Assuming all the samples are uncorrelated and follow a normal distribution, the standard uncertainty of the phase-averaged velocity and the Reynolds normal stresses can be calculated as follows (Sciacchitano & Wieneke 2016).

$$\begin{cases} \varepsilon_{u_i} = \sqrt{u_i^2 / N} \\ \varepsilon_{u_i^2} = u_i^2 \cdot \sqrt{2 / N} \end{cases} \quad (i = x, y, z) \quad (\text{A1})$$

As a result, large measurement uncertainty resides in the region with high velocity fluctuation, namely the front vortex ring and the jet shear-layer. The phase-averaged streamwise and wall-normal velocities are used here as representative examples. The peak values of  $\sqrt{u_x^2}$  and  $\sqrt{u_y^2}$  for all the tested cases reach 26.5 m/s and 41.9 m/s respectively. This results in peak measurement uncertainty of 1.18 m/s and 1.88 m/s with regard to  $\overline{U_x}$  and  $\overline{U_y}$ , which are respectively 1.3% and 2.0% of the peak jet velocity (92 m/s, as already be shown in *Section 4.1*). For the Reynolds normal stresses, the relative estimation error is determined to be 6.3%.

The peak-locking error typically stems from the sub-pixel curve fitting in cross-correlation analysis, and cannot be reduced using statistical averaging (Huang et al. 1997). This error increases significantly when the particle image diameter is less than two pixels. For the investigated case (particle image diameter: 2-3 pixels), the peak-locking error has a periodic pattern with typical amplitude of approximately 0.15 pixels (Chen & Katz 2005). Considering a maximum particle displacement of 10 pixels, the peak-locking error yields a measurement uncertainty of 1.5 % of the peak velocity.

The measurement error associated with the finite spatial resolution of PIV is modelled by Scarano (2003). As concluded, this error is proportional to the second-order spatial derivative of the velocity field for a fixed interrogation window size. For the investigated case, the actual velocity field is largely unavailable. However, based on the results shown in Figure 5 (a), the peak measurement error caused by finite spatial resolution is estimated to be 1.1 m/s.

The finite laser sheet thickness imposes a similar spatial-averaging effect on the measured velocity field as the finite interrogation window. This effect is considered by Zong & Kotsonis (2017), and the peak measurement error yielded is modelled as a function of the ratio of laser sheet thickness to orifice diameter. For the investigated case, the peak relative error is estimated to be 8.3 %.

The final error is related to the discharge timing uncertainty. Specifically, due to internal impedance mismatch and non-ideal properties of the discharge power supply, the high-voltage trigger signal is not an ideal square wave and needs a short time to rise to the breakdown voltage. Since the breakdown voltage of spark discharge in the inter-electrode gap is not deterministic, the exact discharge timing fluctuates between pulses. This timing fluctuation is further propagated to the measurement uncertainty of the phase-averaged velocity (Laurendeau et al. 2015). The relationship between the standard deviation of the discharge timing ( $\delta T$ ) and the produced measurement uncertainty ( $\zeta$ ) is derived in Equation (A2), where a local linear approximation is utilized.

$$\zeta = \overline{U}_i(t + \delta T) - \overline{U}_i(t) \approx \frac{\partial \overline{U}_i}{\partial t} \delta T \quad (\text{A2})$$

Based on the results shown in Laurendeau et al. (2015), the standard deviation of  $\delta T$  is estimated as 3  $\mu$ s. Considering a typical jet acceleration time of 100  $\mu$ s and a peak jet velocity of 100 m/s (Zong & Kotsonis 2016b), the peak value of  $\zeta$  is determined to be 3 m/s.

The Euclidean sum of the above five measurement errors defines the total measurement uncertainty. However, it should be noted that each of the five errors is a function of the time delay ( $t$ ) and the three spatial coordinates ( $x, y, z$ ). Accurate estimation of this spatiotemporal total measurement error is far beyond the scope of this study. Considering a worst case that the five measurement errors peak at the same spatial position simultaneously (statistically improbable), the maximum total measurement error in  $\overline{U}_y$  is determined to be 8.6 m/s, 9.4% of the peak jet velocity.

## References

- Adrian, R. J. (2007) Hairpin vortex organization in wall turbulence. *Phys. Fluids*. 19, 041301.
- Amitay, M., Smith, D. R., Kibens, V., Parekh, D. E. & Glezer, A. (2001) Aerodynamic flow control over an unconventional airfoil using synthetic jet actuators. *AIAA J.* 39, 361–370.
- Anderson, K. V. & Knight, D. D. (2012) Plasma jet for flight control. *AIAA J.* 50, 1855-1872.
- Ashill, P. R., Fulker, J. L. & Hackett, K. C. (2002) Studies of flows induced by sub boundary layer vortex generators (SBVGs). *AIAA 2002-968*.
- Belinger, A., Hardy, P., Barricau, P., Cambronne, J. P. & Caruana, D. (2011) Influence of the energy dissipation rate in the discharge of a plasma synthetic jet actuator. *J. Phys. D: Appl. Phys.* 44, 365201.
- Bernardini, M., Pirozzoli, S. & Orlandi, P. (2014) Velocity statistics in turbulent channel flow up to  $Re_\tau=4000$ . *J. Fluid Mech.* 742, 171-191.
- Bons, J. P., Sondergaard, R. & Rivir, R. B. (1999) Control of low-pressure turbine separation using vortex generator jets. *AIAA Paper*. 1999-0367.
- Broadwell, J. E. & Breidenthal, R. E. (1984) Structure and mixing of a transverse jet in incompressible flow. *J. Fluid Mech.* 148, 405–412.
- Buren, T. V., Beyar, M., Leong, C. M. & Amitay, M. (2016a) Three-dimensional interaction of a finite-span synthetic jet in a crossflow. *Phys. Fluids*. 28, 037105.
- Buren, T. V., Leong, C. M., Whalen, E. & Amitay, M. (2016b) Impact of orifice orientation on a finite-span synthetic jet interaction with a crossflow. *Phys. Fluids*. 28, 037106.
- Buren, T. V., Whalen, E. & Amitay, M. (2016) Achieving a high-speed and momentum synthetic jet actuator. *J. Aerosp. Eng.* 29(2), 04015040.
- Cantwell, B. J. (1986) Viscous starting jets. *J. Fluid Mech.* 173, 159-189.
- Caruana, D., Rogier, F., Dufour, G. & Gleyzes, C. (2013) The plasma synthetic jet actuator, physics, modeling and flow control application on separation. *Aerosp. Lab.* June, 1–13.
- Cater, J. E. & Soria, J. (2002) The evolution of round zero-net-mass-flux jets. *J. Fluid Mech.* 472, 167-200.
- Chen, J. & Katz, J. (2005) Elimination of peak-locking error in PIV analysis using the correlation mapping method. *Meas. Sci. Technol.* 16, 1605-1618.
- Compton, D. A. & Johnston, J. P. (1992) Streamwise vortex production by pitched and skewed jets in a turbulent boundary layer. *AIAA J.* 30, 640–647.
- Cortelezzi, L. & Karagozian, A. R. (2001) On the formation of the counter-rotating vortex pair in transverse jets. *J. Fluid Mech.* 446, 347–373.
- Crittenden, T. M. & Glezer, A. (2006) A high-speed, compressible synthetic jet. *Phys. Fluids*. 18, 017107.
- Emerick, T., Ali, M. Y., Foster, C., Alvi, F. S. & Popkin S. (2014) SparkJet characterizations in quiescent and supersonic flow fields. *Exp. Fluids*. 55, 1858.

- Fuller, E. J., Mays, R. B., Thomas, R. H. & Schetz, J. A. (1992) Mixing studies of helium in air at high supersonic speeds. *AIAA J.* 30, 2234-2243.
- Glezer, A. & Amitay, M. (2002) Synthetic jets. *Annu. Rev. Fluid Mech.* 34, 503–529.
- Greene, B. R., Clemens, N. T., Magari, P. & Micka, D. (2015) Control of mean separation in shock boundary layer interaction using pulsed plasma jets. *Shock Waves.* 25, 495–505.
- Golbabaei-Asl, M., Knight, D. & Wilkinson, S. (2015) Novel technique to determine sparkjet efficiency. *AIAA J.* 53, 501–504.
- Gomes, L. (2009) On the modelling of anisotropic piezoelectric diaphragms for the development of high subsonic synthetic jet actuators. Ph.D. thesis, Univ. of Manchester, Manchester, U.K.
- Grossman, K. R., Cybyk, B. Z. & VanWie, D. M. (2003) Spark jet actuators for flow control. *AIAA Paper* 2003-57.
- Gutmark, E. J., Ibrahim, I. M. & Murugappan, S. (2011) Dynamics of single and twin circular jets in cross flow. *Exp. Fluids.* 50, 653-663.
- Huang, H., Dabiri, D. & Gharib, M. (1997) On errors of digital particle image velocimetry. *Meas. Sci. Technol.* 8, 1427–1440.
- Johnston, J. P. & Nishi, M. (1990) Vortex generator jets: means for flow separation control. *AIAA Journal*, 28, 989–994.
- Kamotani, Y. & Greber, I. (1972) Experiments on turbulent jet in a crossflow. *AIAA J.* 10, 1425–29.
- Karagozian, A. R. (2010) Transverse jets and their control. *Prog. Energ. Combust.* 36, 531-553.
- Kelso, R. M., Lim, T. T. & Perry, A. E. (1996) An experimental study of round jets in cross-flow. *J. Fluid Mech.* 306, 111-144.
- Kline, S. J., Coles, D. E. & Hirst, E. A. (1969) Computation of turbulent boundary layers-1968 AFOSR-IFP-Stanford Conference: proceedings. In *Conference on Computation of Turbulent Boundary Layers*, Stanford University.
- Ko, H. S., Haack, S. J., Land, H. B., Cybyk, B., Katz, J. & Kim, H. J. (2010) Analysis of flow distribution from high-speed flow actuator using particle image velocimetry and digital speckle tomography. *Flow Meas. Instrum.* 21, 443-453
- Krajnovic, S. & Davidson, L. (2002) Large-eddy simulation of the flow around a bluff body. *AIAA J.* 40, 927-936.
- Laurendeau, F., Leon, O., Chedeveigne, F. & Casalis, G. (2015) PIV and electric characterization of a plasma synthetic jet actuator. *AIAA Paper* 2015-2465.
- Mahesh, K. (2013) The interaction of jets with crossflow. *Annu. Rev. Fluid Mech.* 45, 379–407.
- Margason, R. J. (1993) Fifty years of jet in crossflow research. In *computational and experimental assessment of jets in cross flow*. AGARD-CP-534, Winchester, UK.
- Marzouk, Y. M. & Ghoniem, A. F. (2007) Vorticity structure and evolution in a transverse jet. *J. Fluid Mech.* 575, 267-305.
- Meyer K. E., Pedersen J. M. & Oktayozcan. (2007) A turbulent jet in crossflow analyzed with proper orthogonal decomposition. *J. Fluid Mech.* 583, 199-227.
- Narayanaswamy, V., Raja, L. L. & Clemens, N. T. (2010) Characterization of a high-frequency pulsed-plasma jet actuator for supersonic flow control. *AIAA J.* 48, 297-305.

- Narayanaswamy, V., Rajia, L. L. & Clemens, N. T. (2012) Control of unsteadiness of a shock wave/turbulent boundary layer interaction by using a pulsed-plasma-jet actuator. *Phys. Fluids*. 24, 076101.
- Pullin, D. L. (1979) Vortex ring formation at tube and orifice openings. *Phys. Fluids*. 22, 401–403.
- Scarano, F. (2003) Theory of non-isotropic spatial resolution in PIV. *Exp. Fluids*. 35, 268–277.
- Schlichting, H. (1979) *Boundary layer theory*, 7th edition. McGraw-Hill, New York, pp.135–144.
- Sciacchitano, A. & Wieneke, B. (2016) PIV uncertainty propagation. *Meas. Sci. Technol.* 27, 084006.
- Seifert, A., Darabi, A. & Wygnanski, I. (1996) Delay of airfoil stall by periodic excitation. *J. Aircraft*. 33, 691–698.
- Shin, J. (2010) Characteristics of high speed electro-thermal jet activated by pulsed DC discharge. *Chin. J. Aeronaut.* 23, 518–522.
- Smith, B. L. & Glezer, A. (1998) The formation and evolution of synthetic jets. *Phys. Fluids*. 10, 2281–2297.
- Smith, D. R. (2002) Interaction of a synthetic jet with a crossflow boundary layer. *AIAA J.* 40, 2277–2288.
- Smith, S. H. & Mungal, M. G. (1998) Mixing, structure and scaling of the jet in cross-flow. *J. Fluid Mech.* 357: 83–122
- Wang, L., Xia, Z. X., Luo, Z. B. & Chen, J. (2014) Three-electrode plasma synthetic jet actuator for high-speed flow control. *AIAA J.* 52, 879–882.
- Wen, X. & Tang, H. (2014) On hairpin vortices induced by circular synthetic jets in laminar and turbulent boundary layers. *Comput. Fluids*. 95, 1–18.
- Wu, J. Z., Ma, H. Y. & Zhou, M. D. (2007) *Vorticity and vortex dynamics*. Springer, Berlin, ch6.
- Wu, X. & Moin, P. (2009) Direct numerical simulation of turbulence in a nominally zero-pressure-gradient flat-plate boundary layer. *J. Fluid Mech.* 630, 5–41.
- Yuan, L. L. & Street, R. L. (1998) Trajectory and entrainment of a round jet in crossflow. *Phys. Fluids*. 10, 2323–2335.
- Yuan, L. L., Street, R. L. & Ferziger, J. H. (1999) Large-eddy simulations of a round jet in crossflow. *J. Fluid Mech.* 379, 71–104.
- Zong, H. & Kotsonis, M. (2016a) Characterisation of plasma synthetic jet actuators in quiescent flow. *J. Phys. D: Appl. Phys.* 49, 335202.
- Zong, H. & Kotsonis, M. (2016b) Electro-mechanical efficiency of plasma synthetic jet actuator driven by capacitive discharge. *J. Phys. D: Appl. Phys.* 49, 455201.
- Zong, H. & Kotsonis, M. (2017) Effect of slotted exit orifice on performance of plasma synthetic jet actuator. *Exp. Fluids*. 58:17.
- Zong, H., Wu, Y., Li, Y., Song, H., Zhang, Z. & Jia, M. (2015) Analytic model and frequency characteristics of plasma synthetic jet actuator. *Phys. Fluids*. 27, 027105.
- Zong, H., Wu, Y., Song, H. & Jia, M. (2016) Efficiency characteristic of plasma synthetic jet actuator driven by pulsed direct-current discharge. *AIAA J.* 54, 3409–3420.